Particle production in high-energy nuclear collisions: Parton cascade–cluster hadronization model

Klaus Geiger
School of Physics and Astronomy, University of Minnesota, Minneapolis, Minnesota 55455
(Received 19 August 1992)

A phenomenological cluster hadronization scheme for partons in nuclear collisions is presented and combined with the earlier developed parton cascade model to provide a comprehensive description of highly relativistic hadron-hadron and nucleus-nucleus collisions. The model as a whole allows one to study the time evolution of the collisions in complete phase space from the instant of nuclear contact, via the perturbative QCD evolution of parton distributions, to the formation of final hadronic states. The application of this approach to $p\bar{p}$ collisions at $\sqrt{s} = 200$–1800 GeV yields a decent agreement with the experimentally measured momentum and multiplicity distributions. Heavy ion collisions are illustratively studied in the case of central Au + Au collisions at energies of the BNL Relativistic Heavy Ion Collider (RHIC) ($\sqrt{s} = 200A$ GeV) and the CERN Large Hadron Collider (LHC) ($\sqrt{s} = 6300A$ GeV). The impact of a number of nuclear and medium effects on the inclusive hadron production is analyzed and predictions for charged particle spectra and multiplicities are given. In particular, the model results for the central rapidity densities of charged particles are $\simeq 1200$ ($\sqrt{s} = 200A$ GeV) and $\simeq 2500$ ($\sqrt{s} = 6300A$ GeV), which is a factor of ~ 2.5 per nucleon larger than in $p + p$ collisions at corresponding energies.

PACS number(s): 12.38.Mh, 13.87.Fh, 24.85.+p, 25.75.+r

I. INTRODUCTION

The future collider experiments on nucleus-nucleus ($A + A$) collisions at highly relativistic energies ($\sqrt{s} \geq 200A$ GeV) at the BNL Relativistic Heavy Ion Collider (RHIC) and the CERN Lepton Hadron Collider (LHC) offer an opportunity to study ultradense matter in the laboratory and to learn about the new physics that hopefully becomes observable in these reactions. In particular, among the main goals are the search for evidence of the predicted phase transition to a quark-gluon plasma [1]; the confirmation of the expected dominant role of QCD minijet production [2–5] for the reaction dynamics; and the observation of a number of novel nuclear effects on the parton level, for example nuclear shadowing and jet quenching [2,3], as well as medium effects, such as enhanced parton fusion and absorption or the Landau-Pomeranchuk effect [5].

In Ref. [4] a parton cascade model was proposed to study the time evolution of the parton phase-space distributions in ultrarelativistic nuclear collisions. The space-time description is formulated within renormalization-group-improved QCD perturbation theory, embedded in the framework of relativistic transport theory. The dynamics of the dissipative processes during the early stage of the nuclear reactions is simulated as the evolution of multiple internetted parton cascades associated with quark and gluon interactions. In Ref. [5] the model was improved and extended to include a number of new effects that are expected to be of importance in heavy ion collisions, and the implications for the characteristic space-time evolution of partons in these collisions were analyzed. In Ref. [6] the model was applied to study the question of quark-gluon plasma formation and entropy production at RHIC and LHC. Up to now, there was a missing link between the perturbative QCD parton cascade description and the observable final hadron yield, due to the absence of a hadronization prescription. In this paper I will introduce a phenomenological hadronization scheme that models the nonperturbative recombination of partons to clusters at the end of the perturbative evolution and the conversion of these clusters into final hadrons. This cluster hadronization is particularly designed and adjusted to transform the specific final parton configuration of the cascade development into hadronic states. The underlying picture of the hadronization mechanism is rather different from the independent fragmentation approach [7] or the Lund string model [8], the two most commonly used schemes in many event generators for hadronic and nuclear collisions. Instead it is motivated by the "preconfinement" [9] property of partons, which is the tendency of the quarks and gluons produced in the parton cascades to arrange in color neutral clusters already at the perturbative level [10,11]. This concept has been very successfully applied to QCD jet production in e^+e^- annihilation [12–14], and to deep inelastic scattering, the Drell-Yan process as well as to the simulation of hadronic ($p\bar{p}$) collisions [15]. The cluster hadronization scheme introduced in the present paper for nuclear collisions is based essentially on the works of Gottschalk [13] and Webber [14].

This paper is organized in terms of two main parts. The first part, consisting of Secs. II and III, gives a comprehensive outline of the model framework which is intended to provide a realistic simulation of the space-time development of high-energy nuclear collisions. In Sec. II the parton cascade model is reviewed. Here the emphasis is on pointing out the well defined domain of perturbative

cascade development which is bounded by an invariant mass scale μ_0 beyond which nonperturbative hadronization mechanisms are assumed to take over. The newly included cluster hadronization scheme, that is linked to the parton cascade model at this critical scale μ_0, is subsequently introduced in detail in Sec. III. The combined parton cascade–cluster hadronization model simulates hadron-hadron, hadron-nucleus or nucleus-nucleus collisions from the instant of overlap to the yield of hadrons at the end of the reactions. It consists of four major building blocks, each of which is illustrated schematically in Fig. 1:

(i) Phenomenological construction of the initial state in terms of the partons' phase-space distributions in the incoming nuclei (or hadrons) on the basis of the experimentally measured nucleon structure functions and elastic form-factors.

(ii) Time development of parton cascades in complete six-dimensional phase-space according to a semiclassical, relativistic transport equation with a collision kernel that contains the asymptotically dominant perturbative QCD interaction processes among the partons.

(iii) Formation of color neutral clusters from the ensemble of final partons at the end of the perturbative QCD phase for both the secondary produced partons in the central region and the spectator partons in the beam fragmentation region.

(iv) Independent hadronization of each cluster through isotropic two-body decay yielding primary hadron resonances which subsequently decay into final hadrons according to the particle data tables.

The second part of the paper, Sec. II, is devoted to applications and results of the parton cascade–cluster hadronization model. The sensitivity of the model to the invariant mass scale μ_0 and the QCD scale Λ is studied and these two fundamental parameters are fixed by comparison with e^+e^- data. With the parameters determined the model is then applied to high energy $p\bar{p}$

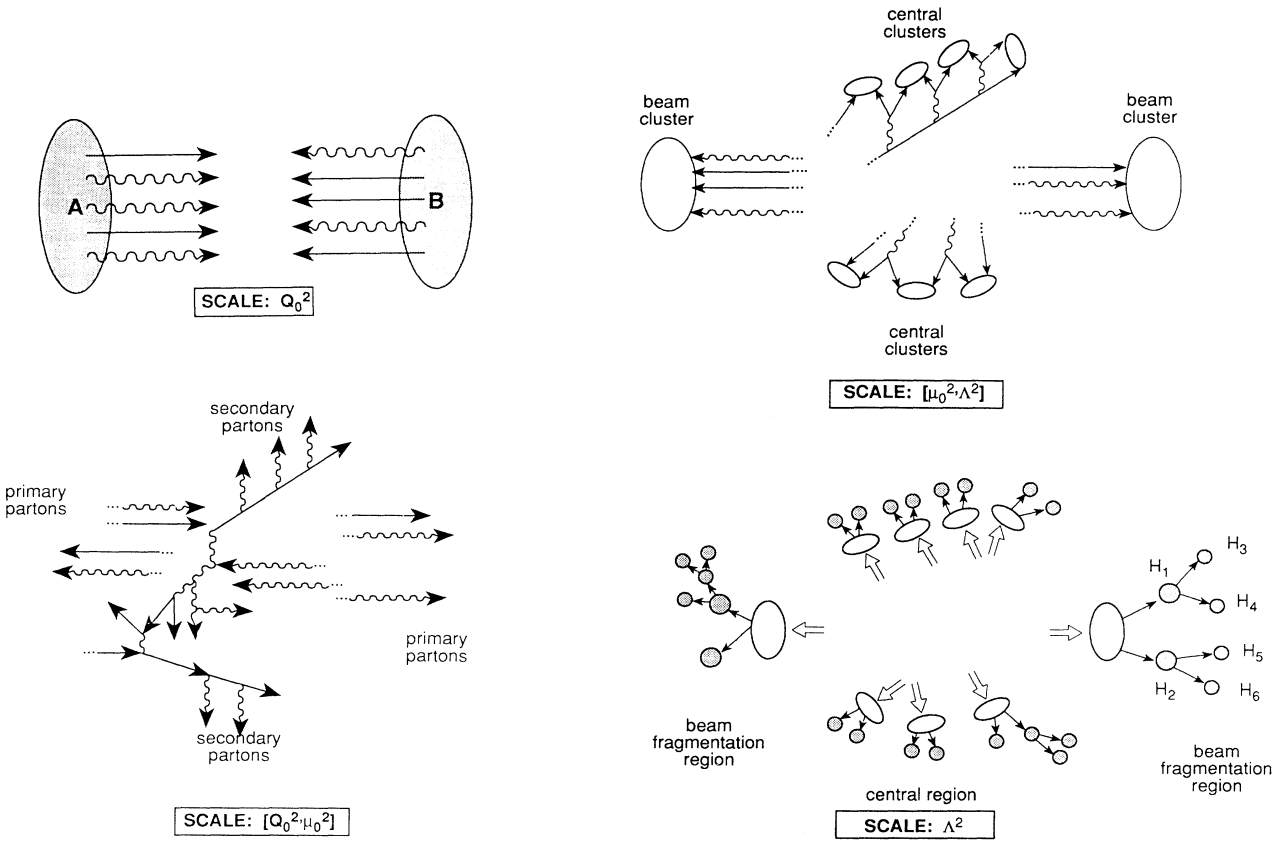

FIG. 1. The four components of the parton cascade–cluster hadronization model: (a) the initial state constructed in terms of the parton distribution of the incoming nuclei at a resolution scale Q_0; (b) the evolution of parton cascades in phase space and time within the perturbative QCD domain between Q_0 and the cutoff μ_0; (c) the formation of color neutral clusters from the final state partons at the end of the perturbative evolution at μ_0; (d) the fragmentation of the clusters as decays into final hadrons at the fundamental QCD scale Λ.

collisions and confronted with data of the CERN and Tevatron collider experiments ($\sqrt{s}$ = 200–1800 GeV). Connecting to this, an investigative study of the hadron production in central Au + Au collisions at $\sqrt{s} = 200A$ GeV (RHIC) and $\sqrt{s} = 6300A$ GeV (LHC) is carried out. Novel effects associated with the massive and dense nuclear collision system are analysed and the momentum spectra of final charged hadrons are compared with those in $p\bar{p}$ and pp collisions [16]. Finally, Sec. V is reserved for summarizing remarks and conclusions.

At this point I would like to emphasize that the parton cascade–cluster hadronization model advocated in this paper is not intended to provide another event generator for high energy nuclear collisions, although it proves to be decently sucessful in reproducing the gross features of hadronic spectra and multiplicities measured in hadron colliders. Its applicability is clearly restricted to ultra-relativistic energies, since it is based on the premise that the dynamics of these reactions can well be described in terms of a kinetic description within the framework of perturbative QCD. Like in most related models there are some crucial assumptions involved and a number of conceptual questions are yet unresolved. A critical discussion of these issues is given in Ref. [5]. Nevertheless, the major advantage of this model lies in the opportunity to study the time evolution of nuclear collisions in complete six-dimensional phase space, from the moment of nuclear touch to the final hadron formation and to investigate how, on the parton level, the properties of perturbative QCD, of nuclear and medium effects are reflected by the hadron production. I would like to note that many other models for high energy nuclear collisions have been developed, e.g., HIJING [2], FRITIOF [17], ATTILA [18], VENUS [19], RQMD [20], QGSM [21], HIJET [22], SPACER [23] and DTUJET [24]. Of these event generators presently only HIJING also incorporates the perturbative QCD approach to multiple minijet production, however within a different framework than in the parton cascade model of the present paper. All other mentioned models rely essentially on the applicability of soft physics descriptions in terms of phenomenological string interactions and fragmentation, even up to collider energies.

II. THE PARTON CASCADE MODEL

Although the general concept and the various physical elements of the perturbative evolution of parton cascades in nuclear collisions have been presented in detail in [4,5], it is conducive for the coherent understanding of the complete model to recall the central aspects of the kinetic description. In the following I will review the most important elements exemplarily for the case of nucleus-nucleus collisions $A+B \rightarrow$ hadrons. For hadron-nucleus or hadron-hadron collisions the replacement of one or both of the beam nuclei by a single hadron is straightforward.

A. The initial state

In the overall center-of-mass frame where the two incoming nuclei A and B and their constituent nucleons are moving close to the speed of light, the parton picture [25,26] is applicable and the parton substructure of the nucleons is resolved at some small resolution scale Q_0. This resolution scale is generally beam energy dependent and is taken to be the statistically estimated expectation value for the interaction scale Q of all primary parton-parton collisions, those in which at least one initial state parton is evolved:

$$Q_0^2(s) = \langle Q^2_{\text{prim.coll.}} \rangle \quad . \tag{1}$$

Here $s = E^2_{\text{c.m.}}$ is the total squared center-of-mass energy of the colliding nuclei and the choice for the scale associated with each primary parton scattering is $Q^2 \equiv p_\perp^2$, with $p_\perp$ the relative transverse momentum of the parton pair. The scale Q_0 defines the initial point in momentum space beyond which the system of partons is evolved perturbatively. The dynamics prior to this point is absorbed in the initial phase-space distributions of the partons, which is constructed as the following superposition of the distribution in the individual nucleons at Q_0 and at time $t = t_0$ when the two nuclei begin to overlap:

$$F_a^{(0)}(Q_0^2; p, r) = \sum_{i=1}^{N_{\text{nuc}}} P_a^{N_i}(Q_0^2; \mathbf{p}, \mathbf{P}) R_a^{N_i}(\mathbf{p}, \mathbf{r}, \mathbf{R})\Big|_{t=t_0} \quad . \tag{2}$$

The notation introduced here is: The right hand side is a sum over all $N_{\text{nuc}} = N_A + N_B$ nucleons of the incoming nuclei A and B, each with a parton distribution given by a convolution of an initial momentum distribution $P_a^{N_i}$ and a spatial distribution $R_a^{N_i}$. The subscript $a = g, q_f, \bar{q}_f$ labels the species of parton (gluons, quarks, or antiquarks of five flavors f) and N_i refers to the type of the ith nucleon, proton or neutron. The four-vectors $p \equiv p^\mu = (E, \mathbf{p})$ and $r \equiv r^\mu = (t, \mathbf{r})$ refer to the partons' momenta and correlated space-time positions and $\mathbf{P}$, $\mathbf{R}$ are the nucleons' momenta and positions, all with respect to the overall center-of-mass frame, at time $t = t_0$. The partons' energies $E \equiv E_a(q^2) = \sqrt{\mathbf{p}^2 + m_a^2 + q^2(Q_0^2)}$ take into account their initial space-like virtualities $q^2(Q_0^2) < 0$, with the constraint that for each nucleon seperately their total invariant mass equals the nucleon mass. This mimics the fact that the partons are off mass shell to some (small) degree, because they are originally confined inside their parent nucleons and cannot be treated as free particles.

As an addition to the earlier work [5], nuclear shadowing effects are now accounted for in the initial phase-space distribution (2). This shadowing of soft partons in a nucleus is evident in the observations of the European Muon Collaboration [27] as a depletion of the nuclear structure functions at small x relative to the ones of a free nucleon. Several mechanisms have been proposed to explain this nuclear shadowing effect on the basis of the parton model [28–31]. To incorporate this phenomenon, I adopt the approach of Ref. [2] and employ the following parametrization [29,31] of the A dependence of the shadowing for both quarks and gluons:

$$\rho_a^A(x) \equiv \frac{f_a^{A,N_i}(x,Q_0^2)}{A\, f_a^{N_i}(x,Q_0^2)}$$
$$= 1 + 1.19\ln^{1/6}(A)\,\left[x^3 - 1.5(x_0+x_L)x^2 + 3x_0x_Lx\right] - \left[\alpha_A(r) - \frac{1.08(A^{1/3}-1)}{\ln(A+1)}\sqrt{x}\right]\exp(-x^2/x_0^2) \quad , \qquad (3)$$

where $f_a^{A,N}$ and f_a^N are, respectively, structure functions of a nucleus A and of a free nucleon, and $x_0 = 0.1$, $x_L = 0.7$. The function

$$\alpha_A(r) \;=\; 0.1(A^{1/3}-1)\frac{4}{3}\sqrt{1-\frac{r^2}{R_A^2}} \qquad (4)$$

takes into account the impact parameter dependence, with r labeling the transverse distance of a nucleon from its nucleus center and R_A the radius of the nucleus.

The initial phase-space distribution $F_a^{(0)}$ of partons a and consequently the total distribution $F^{(0)} = \sum_a F_a^{(0)}$ is generated according to Eq. (2) in the following manner [4,5]:

(i) The nucleons' momenta $\mathbf{P}$ are taken to be equal fractions of the total center-of-mass momentum $\mathcal{P}_{\rm c.m.}$ of their parent nucleus, $\mathbf{P} = (0, 0, \pm\mathcal{P}_{\rm c.m.}/N_{A,B})$, where $+$ $(-)$ refers to the nucleons of nucleus A (B) and N_A (N_B) is the number of nucleons in A (B). The nucleons' energies are taken as $\sqrt{P^2 + M_{\rm nuc}^2}$ and the Fermi motion of the nucleons is neglected. Their positions are initialized in the rest frame of the parent nucleus, around the center of mass of the latter, according to a Gaussian distribution $(2 \le A \le 12)$ or a Fermi distribution $(A > 12)$.

(ii) The partons' longitudinal momenta p_z along the beam direction are sampled from the nuclear structure functions $f_a^{A,N_i}(x,Q_0^2)$ and $f_a^{B,N_i}(x,Q_0^2)$ at the resolution scale Q_0 defined in Eq. (1). They give the probability for finding a parton of type a with a fractional longitudinal momentum $x = p_z/P$ of the ith nucleon N_i in nucleus A, respectively B, where $P = |\mathbf{P}|$. The nuclear structure functions of a nucleus A are parametrized in the form of Eq. (3), that is, $f_a^{A,N_i}(x,Q_0^2) = \rho_a^A(x)\, A\, f_a^{N_i}(x,Q_0^2)$ and similarly for B. For the nucleon structure functions $f_a^{N_i}$ the higher order parametrization of Glück, Reya and Vogt [32] is employed throughout.

Next the primordial transverse momentum $p_\perp = \sqrt{p_x^2 + p_y^2}$ of the partons is chosen according to a Gaussian distribution with $\langle p_\perp \rangle = 0.38$ GeV/c, in accord with experimental analyses [33–35]. The partons' positions within each individual nucleon are assigned in the rest frame of the respective nucleus such that they are distributed around their parent nucleon's center with an exponential distribution $\sim \exp[-\nu r]$ with $\nu = 0.84$ GeV/c corresponding to the elastic form factor of a nucleon with mean square radius $R_{\rm nuc} = \sqrt{12/\nu} = 0.81$ fm.

(iv) Finally, the positions of the nucleons and their valence quarks are boosted from the rest frame of their parent nucleus to the overall center-of-mass frame, which results in a longitudinally Lorentz contracted region $(\Delta z)_v = 2R_{\rm nuc}M_{\rm nuc}/P$ for the valence quarks. The sea quarks and gluons on the other hand are smeared out in the z direction by an amount $(\Delta z)_{s,g} = 1/p_z = 1/xP <$ $2R_{\rm nuc}$ around the valence quarks [36,37]. As a consequence of this implementation of the uncertainty principle the partons' positions are correlated, in longitudinal direction, with their momenta.

The procedure (i)–(iv) yields an initial total phase-space distribution $F^{(0)}(Q_0^2;p,r)$ of partons, summed over all species, that is characterized by two approaching clouds of quarks and gluons, each consisting of a highly Lorentz contracted disc of valence quarks which are surrounded by mostly softer gluons and sea quarks. Note that the number density and the four-momenta of the partons depend considerably on the beam energy, since it determines the longitudinal size of the Lorentz contracted parton clouds and specifies the magnitude of the resolution scale Q_0, Eq. (1), which in turn characterizes the distribution of flavor (a) and momentum (x) among the partons through the scale-dependent nuclear structure functions $f_a^{A,N_i}(x,Q_0^2)$.

B. The perturbative evolution of parton cascades

The time development of the phase-space distribution $F_a(p,r)$ for the partons of species a, starting from its given initial form $F_a^{(0)}(Q_0^2;p,r)$ at time $t = t_0$, Eq. (2), is governed by the relativistic invariant transport equation $(\partial_\mu \equiv \partial/\partial r^\mu)$,

$$p^\mu \partial_\mu F_a(p,r) \;=\; \sum_{\text{processes } k} I_a^{(k)}(p,r) \quad , \qquad (5)$$

with a collision kernel on the right hand side that balances the various processes k by which a parton of type a with four-momentum p and position $\mathbf{r}$ may be gained or lost in a phase-space volume $d^3p d^3r$ around $\mathbf{p}$ and $\mathbf{r}$ at time t. The collision kernel is a sum over Lorentz invariant collision integrals that involve the matrix elements for the different kind of interaction processes in which at least one parton of type a is involved. This specific form of the transport equation is a semiclassical formulation: it describes the evolution of a many-particle system in terms of single-particle distribution functions and classical particle trajectories. The quantum nature of the system is inherent exclusively in the collision term (as will be explained below). The latter models the space-time structure of parton interactions within the framework of renormalization group improved QCD perturbation theory via the relevant matrix elements and takes into account quantum statistical effects by using Fermi-Dirac and Bose-Einstein statistics for quarks and gluons, respectively. Long range color forces are neglected and therefore no color mean field is included. A critical discussion of the assumptions underlying the transport equation (5) and its shortcomings can be found in Ref. [5].

The elementary parton interaction processes included within perturbative QCD are of three types: first, $2 \to 2$ collisions, $a + b \to c + d$; second, $1 \to 2$ branching processes, $c \to a + b$, that produce a parton a; and third, $2 \to 1$ fusion processes, $a + b \to c$, that reduce the number of partons a. Correspondingly the collision kernel in Eq. (5) is represented as

$$\sum_{\text{processes } k} I_a^{(k)}(p,r) = \sum_{b,c,d} \left\{ j^{\text{gain}}_{cd\to ab}(p,r) - j^{\text{loss}}_{ab\to cd}(p,r) \right\} + \sum_{b,c} \left\{ k^{\text{gain}}_{c\to ab}(p,r) - k^{\text{loss}}_{ab\to c}(p,r) \right\} \quad (6)$$

where the functions $j(p,r)$ and $k(p,r)$ are phase-space integrals containing the relevant "effective" matrix elements. Their specific form is given in Ref. [5]. These effective matrix elements are expressed in terms of lowest order perturbative QCD interaction amplitudes which are squared and weighted with a form factor for each of the partons coming in and going out of the vertex. The form factors, which inclusively sum up the higher order corrections associated with the leading logarithmic collinear and infrared singularities of QCD, are taken into account in terms of cascades of both spacelike and timelike partons, as will be explained below.

The time evolution of the partons' phase-space distributions $F_a(p,r)$ according to the transport equation (5) is simulated as a succession of multiple parton-parton collisions together with associated radiative emissions (branchings) and absorption (fusion) processes, once the incoming nuclear parton clouds begin to overlap. The Monte Carlo procedure for this simulation is defined as follows.

1. Parton-parton collisions

Each individual collision between two partons a and b occurs with a probability determined by the invariant total parton-parton cross section that depends on the kinematic variables and the flavors of the pair,

$$\hat{\sigma}_{ab}(\hat{s}) = \sum_{c,d} \left\{ \int_0^{p^2_{\perp\text{cut}}} dp_\perp^2 \left(\frac{d\hat{\sigma}^{\text{soft}}_{ab\to cd}}{dp_\perp^2} \right) + \int_{p^2_{\perp\text{cut}}}^{\infty} dp_\perp^2 \left(\frac{d\hat{\sigma}^{\text{hard}}_{ab\to cd}}{dp_\perp^2} \right) \right\} . \quad (7)$$

Here $p_\perp^2 \simeq \hat{t}\hat{u}/\hat{s}$ is the relative transverse momentum produced, defining the interaction scale $Q^2 \equiv p_\perp^2$, $\hat{s}$, $\hat{t}$, and $\hat{u}$ are the usual Mandelstam variables and the sum over c, d corresponds to summing over all possible reaction channels (processes). The differential cross sections $d\hat{\sigma}^{\text{soft}}_{ab\to cd}/dp_\perp^2$ and $d\hat{\sigma}^{\text{hard}}_{ab\to cd}/dp_\perp^2$ are given in Ref. [4] and Ref. [5], respectively. To render $\hat{\sigma}_{ab}(\hat{s})$ finite, the $p_\perp$ range is divided by an invariant scale $p_{\perp\text{cut}}$ such that for $p_\perp \geq p_{\perp\text{cut}}$ the perturbative QCD cross section $\hat{\sigma}^{\text{hard}}_{ab\to cd}$ is applied, whereas for $p_\perp < p_{\perp\text{cut}}$ a phenomenological, exponentially damped (as $p_\perp \to 0$) soft cross section $\hat{\sigma}^{\text{soft}}_{ab\to cd}$ is employed [5]. The scale $p_{\perp\text{cut}}$ is a parameter of the model that determines how much of the cross section is assigned to truly perturbative QCD processes. Its value generally depends on the beam energy $\sqrt{s}$ of the nuclear collision system $A + B$ and is taken from the following parametrization [38], obtained from an analysis of the measured pp ($p\bar{p}$) cross sections up to TeV collider energies,

$$p_{\perp\text{cut}} = a \left(\frac{\tilde{s}}{s_0} \right)^b , \qquad \sqrt{\tilde{s}} = \frac{2\sqrt{s}}{A+B} , \quad (8)$$

where $a = 0.35$ GeV/c, $b = 0.14$, $s_0 = 1$ GeV^2 and $\tilde{s}$ is the total squared center-of-mass energy normalized to nucleon-nucleon collisions. Next, with $\hat{\sigma}_{ab}(\hat{s})$ determined, then if the closest approach of the partons a and b is within their interaction radius, $|\mathbf{r}_a - \mathbf{r}_b|_{\min} \leq \sqrt{\hat{\sigma}_{ab}(\hat{s})/\pi}$ and the collision occurs, either a (mini)jet with two outgoing timelike partons c and d is produced through $a + b \to c + d$, or else a single virtual parton c emerges via $a + b \to c$. The general type of process, i.e., $2 \to 2$ scattering or $2 \to 1$ fusion, the specific reaction channel and the species of the outgoing partons c and d, or c alone, is determined by the time scale, the interaction scale $p_\perp^2$ and the $\hat{s}$-dependent relative probabilities for the various competing subprocesses. Once the type of process is selected, the kinematics of the collisions, that is the scattering angle and the four-momenta of the outgoing partons, is constructed from the invariants $\hat{s}$, $\hat{t}$, and $\hat{u}$.

The important perturbative QCD radiative corrections associated with the collision $a + b$ occur in two distinct contexts—timelike and spacelike parton cascades—both of which are illustrated in Fig. 2. Each of the secondary quanta c and d emerging from the vertex $a + b \to c + d$ may, subsequent to its production, initiate its own timelike cascade by multiple successive emissions of gluons or branchings into $q\bar{q}$ pairs. Any of these produced partons can either themselves emit additional partons, or absorb an already present close-by parton, or, as a third possibility collide with another parton as decribed before. The evolution of such timelike cascades is followed perturbatively until the typical parton virtuality m^2 falls from the scale $Q^2 = p_\perp^2$ of the collision $a+b$ down to some cutoff μ_0 below which $\alpha_s(m^2)$ becomes too large for perturbation theory. In addition there will also be spacelike parton cascades associated with the incoming partons a and/or b, if one or both of them originate directly from the initial parton clouds of the nuclei without having encountered a collision yet. In this case the colliding partons a and/or b have spacelike virtualities $q^2 < 0$ with $|q^2| \approx Q^2$, resulting from sucessive spacelike branchings that start from the relatively soft scale Q_0^2, Eq. (1), at which these primary partons were originally resolved in the nuclear wave function. Generally three different branchings are possible, $q \to qg$, $g \to gg$, and $g \to q\bar{q}$, which however compete with the reverse absorption processes $qg \to q$, $gg \to g$, and $q\bar{q} \to g$ if the density of surrounding close-by partons is significant, as is the case in heavy ion collisions [5].

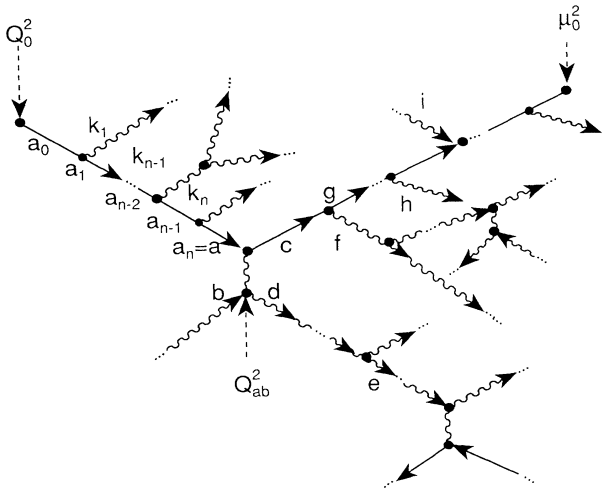

FIG. 2. Schematical illustration of a typical parton cascade development initiated by a collision of two partons a and b. The incoming primary parton a evolves through a spacelike cascade from the initial resolution scale Q_0^2 up to the scale Q_{ab}^2 at which it collides with parton b. The outgoing partons c and d both initiate timelike cascades which are described as a combination of multiple branchings (parton c), absorptions (parton i) or secondary scatterings (parton e). A parton is not allowed to branch further if its virtuality falls below the invariant mass cutoff μ_0. In this case, it propagates freely until it interacts again or finally hadronizes.

2. *Timelike parton cascades*

Consider the timelike cascade initiated by the parton c in Fig. 2. This parton has been produced in the collision $a+b \rightarrow c+d$ with a timelike off-shellness $m_c^2 \simeq Q^2$ ($\equiv Q_{ab}^2$). An "effective" probability $d\mathcal{P}_{cf}^{(T)}$ for the subsequent branching $c \rightarrow fg$ of parton c with virtuality m_c^2 into partons f and g with $m_f^2, m_g^2 < m_c^2$, has been proposed in Ref. [5] as an extension of the standard treatment [39] of the branching process, namely,

$$d\mathcal{P}_{cf}^{(T)}(\xi,z) = \Pi_c(m_c^2,\Delta t)\left(1-\frac{F_f(z,\xi)}{1\pm F_f(z,\xi)}\right) \times \frac{\alpha_s(Q^2)}{2\pi\xi} P_{c\rightarrow fg}(z)dzd\xi \quad , \tag{9}$$

where the + sign refers to parton f being a gluon and the − sign for being a quark. It is formulated in terms of the energy fractions carried by the partons f and g,

$$z = \frac{E_f}{E_c} \quad , \quad 1-z = \frac{E_g}{E_c} \quad , \tag{10}$$

the "angular" evolution variable [10,39,40]

$$\xi = \frac{p_f \cdot p_g}{E_f E_g} \simeq 1-\cos\theta_{fg} \quad , \tag{11}$$

and the virtuality m_c^2 of parton c, which is related to z and ξ through

$$m_c^2 = m_f^2 + m_g^2 + 2E_c^2 z(1-z)\xi \quad . \tag{12}$$

The branching probability (9) consists of three characteristic terms: First, $\Pi_c(m_c^2,\Delta t)$ is the probability that parton c with virtuality m_c^2 and a corresponding "lifetime" $\tau \sim 1/m_c$ decays (branches) within a time interval Δt, taken to be the discrete time steps $\Delta t = 10^{-2}$ fm/c along which the cascade development is followed in time. Second, the term in brackets accounts for the possibility of parton c to absorb a parton f to yield a parton g, that is $c+f \rightarrow g$, rather than to branch into partons f and g via $c \rightarrow f+g$. The relative probability for this to happen is determined by the phase-space density $F_f(z,\xi)$ of partons of species f within $d\xi dz$ around ξ and z. Third, $\alpha_s/(2\pi\xi)P_{c\rightarrow fg}(z)$ is the usual Altarelli-Parisi branching probability [41] associated with the QCD evolution equations, where $P_{c\rightarrow fg}(z)$ is the appropriate branching kernel that describes the energy distribution in the process. The running coupling strength is as usual

$$\alpha_s \equiv \alpha_s(Q^2) = \frac{12\pi}{(33-2n_f)\ln(Q^2/\Lambda^2)} \quad , \tag{13}$$

where Λ is the QCD renormalization scale and n_f the number of quark flavors that can be probed at Q^2. For the branching process $c \rightarrow fg$ described by Eq. (9), the scale Q^2 in $\alpha_s(Q^2)$ is properly chosen as [39,40]

$$Q^2 = 2z^2(1-z)^2 E_c^2 \xi \simeq k_\perp^2 \quad , \tag{14}$$

which is approximately the relative transverse momentum squared between the products f and g at the vertex.

It is important to realize that the specific form of $d\mathcal{P}_{cf}^{(T)}$ in Eq. (9) is based on the "coherent" description of the branching [39] in terms of the variable ξ, taking into account the destructive interference of soft emitted gluons which has been shown to significantly reduce the available phase space for the branching to occur. Furthermore the expression (9) extends the usual description of timelike parton cascades, developed originally for QCD jet studies in e^+e^- annihilation and high energy pp ($p\bar{p}$) collisions, to include two new features that become very important in highly relativistic nucleus-nucleus collisions, as will be shown in Sec. IV C. These are, first, the Landau-Pomeranchuk effect [42] resulting from a finite formation time of radiative gluon emissions (effectively described by the function Π_c), and second, the fact that in heavy ion collisions a dense phase-space occupancy of partons is expected to lead to an enhancement of absorption processes relative to emissions which eventually establishes a detailed balance (expressed by the term in brackets containing the phase-space density F_f of partons f). In addition to the soft gluon interference, both of these latter features also lead to an effective suppression of radiative emissions and consequently to a reduced particle multiplicity. Whereas the time delay of a parton emission connected with the Landau-Pomeranchuk effect allows a parton to rescatter before it is able to radiate, the increasingly probable absorption of partons in dense phase-space regions leads to a decreasing branching probability.

The probability that parton c does *not* branch between ξ and a minimum value $\xi_{\min}$ is given by the exponentiation of (9),

$$T_c(\xi,\xi_{\min}) = \exp\left\{-\int_{\xi_{\min}}^{\xi}\sum_f\int_{z_-(\xi',E_c)}^{z_+(\xi',E_c)} d\mathcal{P}_{cf}^{(T)}(\xi',z)\right\} , \tag{15}$$

called the *Sudakov form factor for timelike branchings.* The cutoffs $\xi_{\min}$ and $z_\pm$ have to be introduced to regularize collinear divergences (in z) and infrared divergences (in ξ). They are determined by the requirement that the branching must terminate when the virtual parton mass m_c^2 drops below some critical invariant scale μ_0^2. This condition leads to a dependence on the cutoff μ_0 as [39]

$$\xi_{\min} = \frac{4\mu_0^2}{E_c^2} \tag{16}$$

and

$$z_+(\xi,E_c) = 1 - z_-(\xi,E_c) = \frac{\mu_0}{\sqrt{\xi}E_c} , \tag{17}$$

so that for $z_+(\xi_{\min},E_c) = z_-(\xi_{\min},E_c) = \frac{1}{2}$ the phase space for the branching vanishes. To specify a process independent cutoff mass μ_0, effective parton masses may be defined as [43]

$$m_{\text{eff}}^{(g)} = \frac{1}{2}\mu_0, \qquad m_{\text{eff}}^{(q)} = \sqrt{\frac{1}{4}\mu_0^2 + m_q^2} , \tag{18}$$

where m_q are the ordinary flavor-dependent current quark masses. The minimum masses for gluons and quarks are then given by

$$\mu_0^{(g)} = 2\,m_{\text{eff}}^{(g)} = \mu_0, \qquad \mu_0^{(q)} = m_{\text{eff}}^{(q)} + m_{\text{eff}}^{(g)} . \tag{19}$$

From (15) it follows that the probability distribution $p_c^{(T)}(\xi_{\max},\xi)$ for parton c to actually branch into partons f and g between ξ and $\xi + d\xi$ with $\xi < \xi_{\max}$ (Fig. 3) is given by

$$p_c^{(T)}(\xi_{\max},\xi)\,d\xi = T_c(\xi_{\max},\xi_{\min})\,\frac{d}{d\xi}\left(\frac{1}{T_c(\xi,\xi_{\min})}\right)d\xi . \tag{20}$$

Here $\xi_{\max}$ is the value of the angular variable of the vertex at which the parton c was produced and is according to Eq. (11) determined by the four-momenta emerging from the vertex. For example, in the case that the parton c originates from a parton-parton collision $a + b \to c + d$ (as in Fig. 2), $\xi = (p_c \cdot p_d)/(E_c E_d)$. The branching is then generated from the distribution $p_c^{(T)}$ by solving for ξ:

$$T_c(\xi,\xi_{\min}) = \frac{T_c(\xi_{\max},\xi_{\min})}{R} , \tag{21}$$

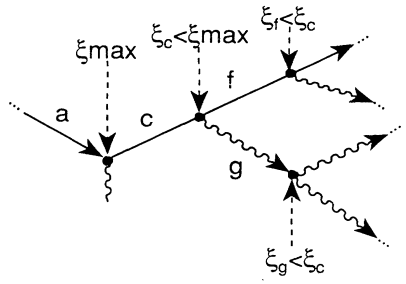

FIG. 3. Angular ordered description of the branching $c \to fg$ in terms of the angular variable ξ, Eq. (11).

with R a random number between 0 and 1. The four-momenta $p_{f,g}^\mu$ and virtualities $m_{f,g}^2 = p_{f,g}^2$ of the daughter partons f and g are then constructed from the chosen values of ξ and z as in Ref. [43]. The partons f and g are subsequently allowed to branch in exactly the same way unless, as stated before, they rescatter or are being absorbed, in which cases the respective branch of the cascade terminates. Furthermore, a perturbative branching process within an individual cascade is forcibly terminated when the virtualities of the partons at a branching vertex fall below the infrared cutoff μ_0. In this case these partons are put on mass shell with effective masses given by Eq. (18) and propagate freely unless they encounter a further collision in which enough energy is transferred to trigger a new cascade.

3. Spacelike parton cascades

Spacelike parton cascades associated with the QCD radiative corrections due to bremsstrahlung emitted by primary spacelike partons that encounter their very first collision and are thereby struck out of the coherent nuclear wave function to become free. The subtle difference between spacelike and timelike parton cascades is that in the former a primary parton evolves from the initial scale Q_0^2 defined in Eq. (1), at which it was originally resolved in the nuclear structure functions, up to the scale Q^2 of the scattering vertex, whereas in the timelike case a secondary parton produced at the vertex of the collision evolves, starting from Q^2, down to the cutoff scale μ_0^2. The evolution of a spacelike cascade is illustrated in Fig. 2, where the parton a_0, originating from the initial nuclear wave function, undergoes successive spacelike branchings $a_0 \to a_1 k_1$, $a_1 \to a_2 k_2$, ..., $a_{n-1} \to a_n k_n$ to become the parton $a \equiv a_n$ which then actually collides with another parton b. The branching chain proceeds by increasing the virtualities of the partons a_i in the cascade, starting from a_0 with $q_0^2 \simeq -Q_0^2$ up to $q^2 \simeq -Q^2$ the spacelike virtuality of the scattering parton a. The partons k_i on the side branches on the other hand have, due to energy-momentum conservation at the branching vertices, timelike virtualities and each of them can initiate a timelike cascade as described before. Although

the simulation of spacelike parton cascades poses special problems [39] not present in the timelike case, these spacelike branchings can also be formulated in terms of a Markov process, similar to the one for timelike branchings, but now involving the initial parton distributions in the incoming nuclei. The generation method used here is the "backward evolution scheme" adopted from Ref. [44], where a detailed presentation can be found. To sketch the procedure, consider the spacelike branching $a_{n-1} \rightarrow a_n k_n$ in Fig. 2, where the virtualities of the partons a_{n-1}, a_n, and k_n are q_{n-1}^2, q_n^2, and p_n^2, respectively, with $|q_n^2| < |q_{n-1}^2|$, and $q_n^2, q_{n-1}^2 < 0$ (spacelike) but $p_n^2 > 0$ (timelike). The relative probability for this branching to occur between Q^2 and $Q^2 + dQ^2$ is given by

$$d\mathcal{P}^{(S)}_{a_{n-1}a_n}(x_{a_{n-1}}, x_{a_n}, Q^2) = \frac{\alpha_s(Q^2)}{2\pi Q^2} \left(\frac{f_{a_{n-1}}(x_{a_{n-1}}, Q^2)}{f_{a_n}(x_{a_n}, Q^2)} \right) \frac{1}{\tilde{z}} P_{a_{n-1}\rightarrow a_n k_n}(\tilde{z})\, dQ^2\, d\tilde{z} \quad . \tag{22}$$

Here $x_\alpha = (p_\alpha)_z/P$ ($\alpha \equiv a_{n-1}, a_n$) are the fractional longitudinal momenta of the parent nucleons carried by the partons a_{n-1} and a_n, the quantity $\tilde{z} = x_{a_n}/x_{a_{n-1}}$ is the fraction of momentum of parton a_n taken away from a_{n-1}, $f_\alpha(x_\alpha, Q^2)$ are the corresponding nucleon structure functions that enter the initial parton distributions (3), and $Q^2 \equiv Q^2_{ab}$ is associated with the scale of the scattering vertex of parton $a_n \equiv a$ colliding with another parton b as in Fig. 2.

The "backwards evolution" of the spacelike branching $a_{n-1} \rightarrow a_n + k_n$ is expressed in terms of the probability that parton a_{n-1} did *not* branch between the lower bound given by the initial resolution scale Q_0^2 and Q^2. In that case parton a_n *cannot* originate from this branching, but must have been produced otherwise or already been present in the initial parton distributions. This nonbranching probability is given by the *Sudakov formfactor for spacelike branchings* [44]:

$$S_{a_n}(x_{a_n}, Q^2, Q_0^2) = \exp\left\{ - \sum_{a_{n-1}} \int_{Q_0^2}^{Q^2} \int_{\tilde{z}_{\min}(Q'^2)}^{\tilde{z}_{\max}(Q'^2)} d\mathcal{P}^{(S)}_{a_n a_{n-1}}(x_{a_n}, \tilde{z}, Q'^2) \right\} \quad . \tag{23}$$

The spacelike branching is then sampled from the corresponding branching probability distribution $p^{(S)}_{a_n}(x_{a_n}, Q^2, Q^2_{\max})$ that the parton a_n actually has emerged from the branching $a_{n-1} \rightarrow a_n + k_n$ between Q^2 and $Q^2 + dQ^2$,

$$p^{(S)}_{a_n}(x_{a_n}, Q^2_{\max}, Q^2)\, dQ^2 = S_{a_n}(x_{a_n}, Q^2_{\max}, Q^2_{\min}) \frac{d}{dQ^2} \left(\frac{1}{S_{a_n}(x_{a_n}, Q^2, Q^2_{\min})} \right) dQ^2 \quad , \tag{24}$$

where $Q^2_{\max}$ specifies the maximum virtuality of parton a_n which is set by the scale of the scattering vertex of $a + b$, and $Q^2_{\min} = Q_0^2$ is the lower bound given by the initial resolution scale (1). Solving the equation

$$S_{a_n}(x_{a_n}, Q^2, Q_0^2) = \frac{S_n(x_{a_n}, Q^2_{\max}, Q_0^2)}{R} \quad , \tag{25}$$

where R is a uniformly distributed random number in $[0, 1]$ determines Q^2. Subsequently the kinematics of the branching is reconstructed as in [44] and the procedure is repeated further backwards with parton a_n replaced by a_{n-1} and $Q^2_{\max}$ replaced by Q^2, and so forth, until the virtualities reach the initial scale Q_0^2.

Note that for the spacelike cascades the evolution variables are the momentum fraction $\tilde{z}$ and the virtuality Q^2, whereas in the timelike case the corresponding variables are chosen to be the energy fraction z and the angular variable ξ. Furthermore, soft gluon interference and the other effects incorporated in the simulation of timelike cascades are neglected for the spacelike cascades, although it has been shown [45] that the destructive interference of low energy gluons can be implemented here by a proper modification of the spacelike Sudakov form factor (23). However, in nuclear collisions the contribution of spacelike cascades to the dynamics of the parton system as a whole turns out to be insignificant relative to the timelike cascades [5], because they are only of relevance for primary partons involved in their first collisions with an interaction scale $Q^2 \gg Q_0^2$. Since the value of Q_0^2 is estimated according to Eq. (1), only rather hard primary scatterings, which are rare fluctuations, give rise to a spacelike cascade. Therefore, the neglect of soft gluon interference as a correction to the spacelike branching processes should be irrelevant for the global dynamics.

III. CLUSTER HADRONIZATION

The perturbative evolution of the ensemble of parton cascades proceeds until the majority of partons have harnessed most of their initial kinetic energy in collisions or branchings and have invariant masses $m \simeq \mu_0$. At this point the residual parton interactions reduce to purely elastic collisions and the system eventually approaches free streaming, with the partons freely moving apart. However, the presence of long range color forces implies that a set of partons can evolve independently only if they form a color singlet system. Therefore the task is to identify appropriate sets of partons which evolve beyond the perturbative cutoff scale μ_0, defined by Eqs. (18) and (19), and separately form hadrons. The important assumption here is that the process of hadron formation

depends only on the local structure of the parton system over small space-time volumes.

The scheme to model the nonperturbative mechanism of hadron formation is based on the approaches of Refs. [12–15]. The central idea is that, at the end of the perturbative phase of parton cascade development, color singlet clusters of partons are formed which subsequently decay independently into hadrons. This concept follows naturally from the "preconfinement" property [11]. Preconfinement is the tendency of the partons produced in the individual cascades to be arranged in color singlet clusters with limited extension in both position and momentum space. It is natural to suppose that these clusters are the basic units out of which hadrons arise nonperturbatively. The preconfinement picture is based on the observation that partons which are correlated in color space due to mutual interactions, have in perturbation theory a damped invariant mass distribution [10] with an average mass of the order of μ_0. The usual approach to identify sets of partons that are "close in color" is to employ a description in terms of color diagrams [14,40] which connect interacting partons among each other and keep track of the color flow in and out of a vertex. Such color connected systems of partons are the minimal color neutral clusters [46] that may be taken to form hadrons independently.

The essential difference between the perturbative evolution of parton cascades in the present model and the approach of Ref. [14] is that the former does *not* make explicit use of the color flow structure of the evolving cascades. Although in principle possible, it is not attempted to determine which partons are nearby in color, because of the tremendous complexity of this problem. However, the crucial connection is the fact that partons which are close in color (in particular minimal color singlets) are also close in phase space [10]. Exploiting this property, the approach adopted here is, instead of using a color flow description, to forget about the color structure during the cascade development. Rather, at the end of the perturbative evolution color neutral clusters are formed from the final partons which have a minimal separation in coordinate and momentum space. The results to be presented in Sec. IV will justify this alternative method and demonstrate the connection between color structure and phase-space occupation of the final parton configuration before hadronization.

A. Cluster formation

In the following I will introduce the phenomenological model for cluster formation from the collection of quarks and gluons at the end of the perturbative phase which consists of two components:

(i) The rearrangement of the secondary partons, being timelike or on mass shell, and their conversion into color singlet clusters ("central clusters").

(ii) The recombination of the primary, spacelike partons that remained spectators throughout the nuclear reaction ("beam clusters").

1. Central clusters

Central clusters are formed from secondary partons. As defined before, the secondary partons are those that have interacted at least once or have been created during the perturbative evolution. The first step in the cluster formation scheme is to forcibly split each secondary gluon into a collinear quark-antiquark pair. It is assumed that this occurs through a nonperturbative enhancement below μ_0 of the splitting $g \to q\bar{q}$, which is relatively uncommon in the perturbative branching. The q and $\bar{q}$ are taken to have momenta uniformly distributed in the allowed range, parallel to the gluon four-momentum. Their flavors are chosen as u, d, or s with equal probabilities as long as the invariant mass of the pair exceeds the kaon mass. This procedure leaves an ensemble of final state quarks and antiquarks which will have to be rearranged to form color singlet clusters. The next step is to employ the preconfinement picture mentioned before: each quark is assigned to an antiquark sibling (distinct from its antiquark partner in the gluon splitting), which is closest to it in phase space and therefore in the average also the closest one in color space. The phase-space distance measure Δ_{ij} between two partons, labeled with indices i and j, is chosen to be

$$\Delta_{ij} = \sqrt{r_{ij}^{\mu}\, r_{ij,\mu}}\ \sqrt{p_{ij}^{\nu}\, p_{ij,\nu}}\ , \tag{26}$$

where $r_{ij} = r_i - r_j$ and $p_{ij} = p_i - p_j$. Of course other measures are possible [47,48]; however, the form (26) has the advantage of being manifestly Lorentz invariant and has the dimension of phase space [49].

Accordingly quark-antiquark clusters $q_i\bar{q}_j$ are formed by measuring for each quark q_i its phase-space separation Δ_{ij} with respect to every antiquark $\bar{q}_j$ and selecting the one that has the minimum distance $\min_j(\Delta_{i1}, \ldots, \Delta_{ij}, \ldots, \Delta_{in})$ to be the sibling antiquark of q_i. This scheme, illustrated in Fig. 4, leads to a particular phase-space distribution of color singlet $q_i\bar{q}_j$ clusters with their four-momenta and positions given by, respectively, the sum of the four-momenta and the centers of mass of the two constituents:

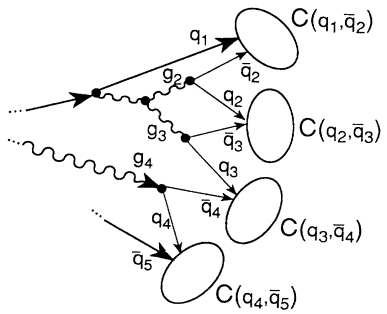

FIG. 4. Illustration of the cluster formation scheme described in Sec. III A. First, final state gluons are split into collinear quark-antiquark pairs. Then color neutral $q_i\bar{q}_j$ clusters are formed from a quark q_i and an antiquark $\bar{q}_j$ with the smallest separation in phase-space.

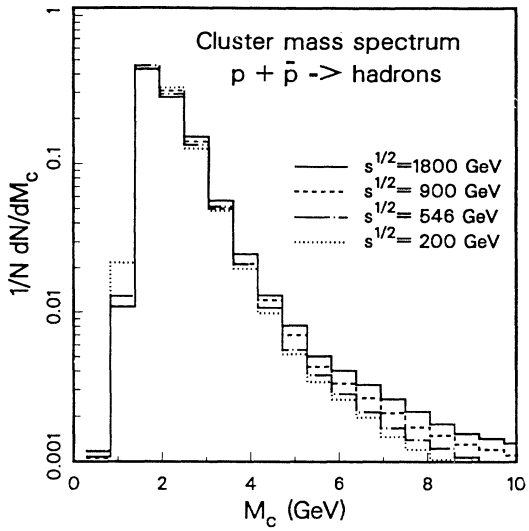

FIG. 5. Invariant mass spectra of central clusters formed according to the procedure of Sec. III A in simulations of $p\bar{p}$ collisions at different beam energies. The parameter values are $\Lambda = 0.4$ GeV, $\mu_0 = 1$ GeV. The distribution is strongly damped above $\sim 2\,\mu_0$ and is roughly independent of the beam energy $\sqrt{s}$.

$$P_c^\mu = p_i^\mu + p_j^\mu \quad , \qquad M_c^2 = P_c^2 \quad , \tag{27}$$

$$\mathbf{R}_c = \frac{m_i \mathbf{r}_i + m_j \mathbf{r}_j}{m_i + m_j} \quad . \tag{28}$$

In Fig. 5 a typical invariant cluster mass distribution calculated for $p\bar{p}$ collisions with various beam energies $\sqrt{s} = 200, 546, 900, 1800$ GeV is shown. It exhibits the characteristic features of preconfinement: the distribution is peaked at low mass, strongly damped at large mass, and is roughly independent of the beam energy.

2. Beam clusters

The remaining fraction of the longitudinal momentum and energy that has not been redirected and harnessed in parton interactions is carried by the primary partons of the initial nuclei. These initial state partons that remained spectators throughout the nuclear collision have maintained their originally assigned momenta and their spacelike virtualities (except for the valence quarks which are on mass shell) and make up the two fast receding beam fronts. Whereas the primary valence quarks represent the baryon number density that remains in the the beam fronts, the spacelike sea quarks and gluons are to be interpreted as virtual excitations of the color field around the valence quarks and therefore must contribute to the internal energy of the beam fragments. They may be pictured as the coherent relics that remained from the original wave functions of the initial nuclei. Therefore the primary virtual partons must be treated differently than the secondary partons which have been scattered out of the coherent initial state and have become real excitations. The prescription used here to convert the primary partons into two beam clusters is a rather simple "nuts and bolts" scheme that proceeds as follows.

With respect to the nuclear center-of-mass frame the primary partons are divided into two sets according to their direction of momentum along the beam axis and their positions. Each set of partons is then assumed to form a beam cluster C_+ (C_-) with positive (negative) longitudinal momentum moving apart from each other on the right (left) side of the center of mass. The cluster four-momenta and masses are evaluated as

$$P_\pm^\mu = \sum_i (p_i^\mu)_{\rm spec}\, \theta(\pm p_z) \quad , \qquad M_\pm = P_\pm^2 \quad , \tag{29}$$

where the sum runs over all spectator partons with $p_z > 0$ ($p_z < 0$), irrespective of their species. The cluster center-of-mass positions are simply taken to be the vector means of the respective partons' positions,

$$\mathbf{R}_\pm = \frac{1}{N_\pm} \sum_i (\mathbf{r}_i)_{\rm spec}\, \theta(\pm z) \quad , \tag{30}$$

where N_+ (N_-) is the number of partons assigned to cluster C_+ (C_-). The total electric charge Q_+ (Q_-) of cluster C_+ (C_-) is determined by its valence quark content. As a consequence of charge conservation, the sum $Q_+ + Q_-$ is necessarily equal to the sum of the charges of the initial nuclei minus the sum of the central cluster charges. However, it may occur that Q_+ and/or Q_- do not meet the physical requirement of being integers. This happens when an unbalanced number of valence quarks has scattered during the collision so that they are lumped together with the secondary partons in the central clusters. Although the total charge of the system as a whole is still conserved, this leads to unphysical charges of the beam clusters and the system of central clusters separately and also implies that the clusters are not color singlets. To avoid a rejection of (very computational intense) nuclear collision events with such a final parton configuration, the parton content of a beam cluster with unphysical flavor composition is forcibly adjusted as follows. The lowest energy quark or antiquark of the cluster, with appropriate flavor u, $\bar{u}$, d, or $\bar{d}$ to reduce the charge imbalance, is put on mass shell and assigned to the secondary partons in the central region. If necessary, this is repeated with the next lowest energy quark or antiquark. With the available flavors u and d at most two such conversions are required to yield a total integer charge and to ensure the color singlet character of the beam cluster. With this modified parton configuration the complete cluster procedure is then redone.

B. Cluster hadronization

1. Central clusters

The invariant mass distribution of central clusters (Fig. 5) may be interpreted as a "smeared out" version of the spectrum of primordial resonances formed in the early stages of the confinement mechanism [10]. It seems therefore reasonable to treat the fragmentation of these central

clusters as a kind of averaged resonance decay which, as implied by the locality assumption, must be determined entirely by their invariant masses, flavors, and total angular momentum. Each cluster in the resonance spectrum may either represent a single hadron resonance that converts directly into a physical hadron with a definite mass, or else fragments through a two-body decay into a pair of final state hadrons. From the particle spectra obtained in e^+e^--annihilation experiments it appears that quasi-two-body final states are universally dominant, so that the latter possibility seems more favorable if kinematically allowed.

The hadronization scheme for the central clusters employed here follows closely the scheme of Marchesini and Webber [15]. Three regions of cluster mass have to be distinguished, each of which is illustrated in Fig. 6:

(i) Any cluster C that is too light to decay into two hadrons is taken to represent the lightest single hadron (meson) H of its flavor,

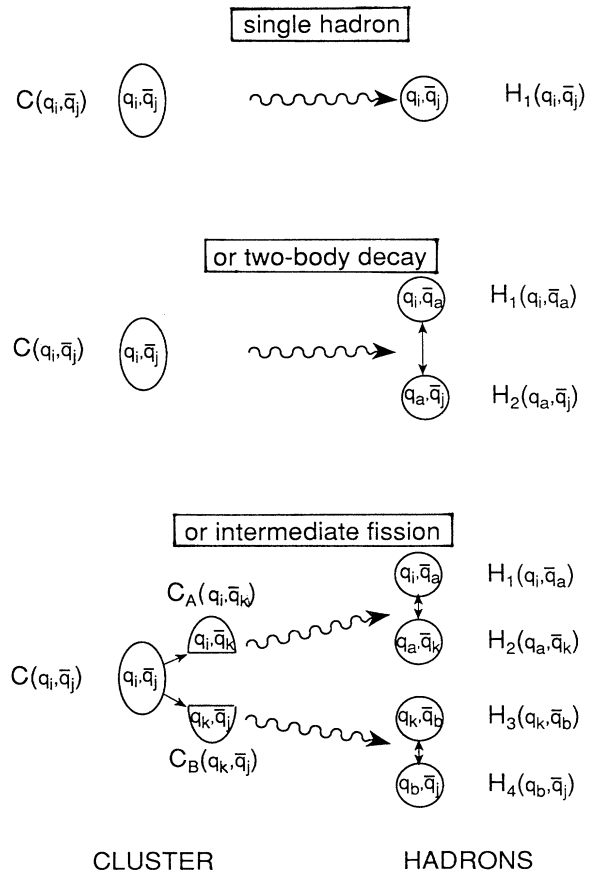

FIG. 6. Illustration of the cluster fragmentation prescription of Sec. III B. Each cluster is allowed to convert into a single hadron (if the invariant mass is small enough) or to "decay" isotropically in its rest frame into two hadrons. However, very massive clusters are assumed to successively fission first, until their masses fall below a fission threshold, before they transform into hadrons.

$$C(q_i\bar{q}_j) \longrightarrow H(q_i,\bar{q}_j) \tag{31}$$

with its mass shifted to the appropriate value by adjusting its energy through exchange with a neighboring cluster.

(ii) Each cluster massive enough to decay, but below a fission threshold [specified in (iii) below] decays isotropically in its rest frame into a pair of hadrons as

$$C(q_i\bar{q}_j) \longrightarrow H_1(q_i,\bar{q}_a) + H_2(q_a,\bar{q}_j) \tag{32}$$

or as

$$C(q_i\bar{q}_j) \longrightarrow H_1(q_i,q_aq_b) + H_2(\bar{q}_a\bar{q}_b,\bar{q}_j) \tag{33}$$

by pulling a quark-antiquark pair $q_a\bar{q}_a$ or a diquark-antidiquark pair $(q_aq_b)(\bar{q}_a\bar{q}_b)$ from the vacuum. These created pairs need not be viewed as physical entities with dynamical attributes. Rather, they function as a label for counting and conserving flavor and baryon number. The model sums over a number of possible decays for each cluster. The probability for a specific decay mode is taken to be a product of a flavor, a spin, and a kinematical factor,

$$\mathcal{P}_{C\to H_1H_2} = P_f(M_c,m_a)\,P_s(J_1,J_2)\,P_k(M_c,M_1,M_2) \ , \tag{34}$$

where M_c is the cluster mass, m_a (m_{ab}) the flavor dependent quark (diquark) mass, and $J_{1,2}$ and $M_{1,2}$ are, respectively, the angular momenta and masses of the two hadrons $H_{1,2}$. The flavor factor

$$P_f(M_c,m_a) = \left(1+\frac{2m_a^2}{M_c^2}\right)\sqrt{1-\frac{4m_a^2}{M_c^2}} \tag{35}$$

is the two-body phase-space suppression function for the decay of an object of mass M_c into a $q_a\bar{q}_a$ or $(q_aq_b)(\bar{q}_a\bar{q}_b)$ pair. The flavors are restricted to be $a = u,\ d,\ s,\ c$ for $q_a\bar{q}_a$ and $ab = uu,\ ud,\ us,\ dd,\ ds$, and ss for $(q_aq_b)(\bar{q}_a\bar{q}_b)$, with $m_u = 5.6$ MeV, $m_d = 9.9$ MeV, $m_s = 199$ MeV, and $m_c = 1.35$ GeV. The diquark masses are taken to be $m_{ab} = m_a + m_b$. The spin factor

$$P_s(J_1,J_2) = (2J_1+1)\,(2J_2+1) \tag{36}$$

takes into account the spin degeneracy with the allowed spins J_1 and J_2 of the two hadrons depending on their quark contents. For hadrons that contain only u, d, s flavors, the allowed states are $J^P = 0^-, 1^\pm, 2^+$ mesons and $J^P = \frac{1}{2}^+, \frac{3}{2}^+$ baryons. The kinematic factor

$$P_k(M_c,M_1,M_2) = \frac{\sqrt{\lambda(M_c^2,M_1^2,M_2^2)}}{M_c^2} \tag{37}$$

is simply the two-body phase-space factor, where

$$\lambda(a,b,c) = a^2+b^2+c^2-2\,(ab+ac+bc) \ . \tag{38}$$

(iii) Occasionally the final state parton configuration yields clusters with masses that are too large for an isotropic decay to be a reasonable ansatz. Even though the mass spectrum falls rapidly at large masses (Fig. 5), a small fraction (about 5–10 %) of the clusters have masses $M_c > 4$ GeV. These clusters are fragmented by using the

iterative fission model proposed in Ref. [14]. For a cluster of mass $M_c > M_{\rm fiss}$, where $M_{\rm fiss}$ is the fission threshold, formed from a quark q_i with four-momentum p_i and an antiquark $\bar{q}_j$ with momentum p_j, the fission $C \to A + B$ is assumed to yield

$$P_A^\mu = \left(1 - \frac{\mu_0}{M_c}\right) p_i^\mu + \left(\frac{\mu_0}{M_c}\right) p_j^\mu ,$$
$$P_B^\mu = \left(\frac{\mu_0}{M_c}\right) p_i^\mu + \left(1 - \frac{\mu_0}{M_c}\right) p_j^\mu \quad , \tag{39}$$

where μ_0 is the invariant mass scale (19) that separates the perturbative and nonperturbative domains. This fission mechanism implies $M_A^2 \simeq M_B^2 \simeq \mu_0 M_c$ and may be interpreted as a "symmetrical string breaking" of a string with mass density μ_0 per unit rapidity through the production of a $q\bar{q}$ pair with virtuality of the order of μ_0^2 [14]. The flavor of the produced pair is restricted to be $u\bar{u}$, $d\bar{d}$, or $s\bar{s}$ with equal probability. The procedure is repeated for the fragments A and B until all cluster masses fall below the fission threshold $M_{\rm fiss}$ and isotropic decay continues as explained in (ii).

2. *Beam clusters*

As explained in Sec. III A 2, the two beam clusters that are formed from the spectator partons representing the receding beam fronts carry a significant part of the original longitudinal beam momentum and are characterized by large rapidities. This leads to a specific momentum distribution of final hadrons in the high rapidity region which is assumed to be generated by a soft underlying beam-beam interaction. The fragmentation of the beam clusters proceeds in two steps as follows. First, each of the two clusters is split into an ensemble of collinear nucleons carrying equal fractions of the four-momentum of the cluster. The number of nucleons per beam cluster is determined requirement that the sum of nucleon masses equals the cluster mass. The nucleon species are chosen as protons or neutrons with the same probability. If the sum of the nucleon charges does not match the total cluster charge, then one or more neutrons are replaced by protons or antiprotons until the total charge is adjusted. Next, soft interactions between the nucleons of the incoming nuclei and the nucleons resulting from the beam cluster splitting are assumed to have occurred during the collision. This is modeled as low momentum transfers between pairs of nucleons, each pair consisting of a nucleon from one beam cluster and one from the other cluster to which it is closest in phase space. Each of these pairwise interactions involves a squared momentum transfer t with a distribution corresponding to a diffractive nucleon-nucleon scattering [50],

$$dP(t) = \exp[Bt + Ct^2]dt \ . \tag{40}$$

Here $B \equiv B(s)$ is the nuclear slope parameter and $C \equiv C(s)$ is the curvature parameter taken from the parametrizations of Block and Cahn [51].

The motivation to take into account such a soft beam-beam interaction underlying the reaction dynamics of partons is that this ansatz naturally mimics the structure and number of diffractive events in pp ($p\bar{p}$) collisions (which are the subject of Sec. III B below). In the simulation of these reactions it occasionally happens (especially in peripherical collisions) that the partons of the incoming p and p ($\bar{p}$) pass through each other without any interaction. Such events are then simply pictured as diffractive events as opposed to nondiffractive events. In nondiffractive collisions the coherence of the incoming p and $\bar{p}$ is destroyed in the reaction, because at least one quark or gluon is struck out of each of the nucleons' wave function by a parton-parton interaction. Contrary to that, a single (double) diffractive reaction excites one (both) of the beam particles to a resonant state but by maintains the color singlet coherence of the initial nucleons. Therefore it is natural to identify simulated events with at least one parton-parton collision as nondiffractive events and treat collisions with no parton interactions at all as diffractive events. When proceeding from pp ($p\bar{p}$) to AA collisions the probability for diffractive events becomes very small [38] and only collisions with large impact parameter are affected.

IV. RESULTS AND PHENOMENOLOGY

Before applying the model to nuclear collisions, reasonable values for the two central parameters, the QCD scale Λ and the infrared cutoff μ_0, have to be determined from experimental data. Their dimensionless ratio defines the maximum value of the effective coupling α_s/π, Eq. (13), which can occur in the perturbative cascade evolution of parton branchings. A third parameter is the fission threshold $M_{\rm fiss}$ for the fission of heavy clusters before they decay isotropically. As it turns out, this parameter is, in contrast to Λ and μ_0, of little influence on global observables such as multiplicities and momentum distributions. Finally, the only other essential parameter that affects the structure of the final parton configuration in nuclear collisions is $p_{\perp{\rm cut}}$ in the parton-parton scattering cross section (5) which, however, is independently fixed according to the parametrization (6). Hence, it remains to study the effects of a variation of Λ and μ_0 in order to specify the point where the perturbative evolution of parton cascades is taken over by the nonperturbative hadronization of the final partons. The parameter Λ is the more fundamental one. As will become evident below, for fixed Λ the choice of the parameter μ_0 has the effect that for a larger value the number of produced partons will be smaller and the masses of color neutral clusters will increase, and vice versa. Consequently, a large value yields massive clusters that decay into many hadrons, whereas the choice of a small μ_0 results in many light clusters, each giving only a few hadrons. Since both possibilities are plausible, the actual choice of Λ and μ_0 needs to be determined from the quality of reproducing a broad range of standard experimental measures. Ideally the final hadron distributions should be rather insensitive to the scale μ_0, even though the perturbative and the hadronization scheme separately depend strongly on it, because it only defines the somewhat arbitrary scale

at which the description of the evolution process changes.

I emphasize that the results and comparisons with experimental data presented in the following subsections are not intended to be quantitative tests of perturbative QCD. Indeed, the critical aspect of this work is the cluster fragmentation model for the nonperturbative hadronization. The purpose of this section is to demonstrate that the picture of hadronization as the formation and decay of clusters is quite consistent with the present data and that a broad range of experimental results can be understood without the introduction of fragmentation functions and the necessity of a number of additional parameters. In fact, apart from the cluster fission threshold $M_{\rm fiss}$, no new parameters are introduced to describe the transition from the final parton configuration into hadrons. The aim of Sec. IV A is to fix Λ and μ_0 and to compare with some high statistics e^+e^- event studies, since here initial state partons are absent and parton cascades are initiated by a single $q\bar{q}$ jet, allowing for a transparent analysis. With the parameters fixed, Sec. IV B then presents a comparative study of $p\bar{p}$ collider data with the full model, including initial state partons and the additional fragmentation of beam clusters. In Sec. IV D the model is applied to ultrarelativistic heavy ion collisions, exemplarily to the case of central Au + Au collisions at RHIC and LHC energies, to study the new physics associated with nuclear and medium effects by analyzing the final hadron momentum distributions, and to extract predictive estimates for the charged particle multiplicities.

A. Study of model parameter dependence in e^+e^- annihilation

The most characteristic observable measures to study the significance of a variation of the parameters Λ and μ_0 are the hadron multiplicities and the particle composition of the final state, the transverse momentum, and the rapidity distributions of the produced hadrons. Since parton cascades are most easily, and cleanly, produced in e^+e^- annihilation where perturbative QCD is most transparently disentangled from the hadronization process, I will examine the parameter dependence by comparing the predictions of the model with the very well measured e^+e^- data of PETRA/PEP and LEP [52]. In the past a number of similar investigations have been carried out within the context of QCD jet studies [12–14].

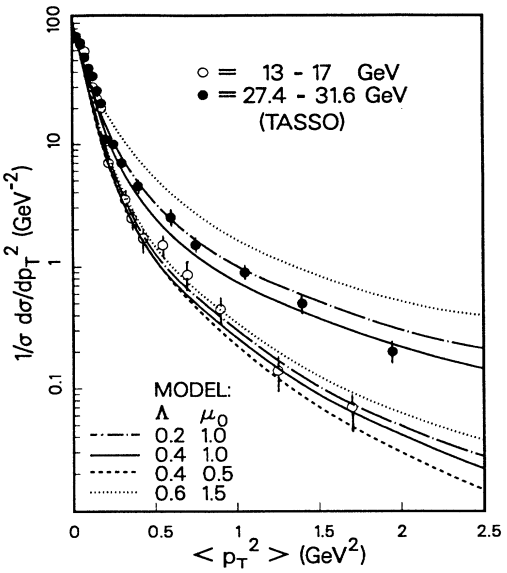

FIG. 7. Transverse momentum distribution of charged particles in simulated e^+e^--annihilation events at $Q = 15$ GeV and $Q = 29$ GeV. The experimental data are from Ref. [56]. Both model results and data are relative to the sphericity axis.

The results of this subsection were obtained by simulating e^+e^- annihilation events as the production of $q\bar{q}$ jets through a virtual γ with invariant mass Q, evolving the jets perturbatively as parton cascades [53] according to Sec. II B, and hadronizing the final partons using the cluster hadronization of Secs. III A and III B. Table I summarizes some characteristic properties of the partons and resulting clusters as calculated with $Q = 34$ GeV, for four different choices of Λ and μ_0. The dependence on Λ, μ_0, and on $M_{\rm fiss}$ of some important observables in e^+e^- annihilation, at $Q = 34$ GeV where there are especially good data, is listed in Table II. One observes that the parameter dependence is generally small. Table I demonstrates the compensation between the perturbative phase of parton cascade development and the hadronization stage for various combinations of Λ and

TABLE I. Dependence of parton and cluster multiplicities on the model parameters Λ and μ_0 in e^+e^- annihilation events at center-of-mass energy $Q = 34$ GeV.

Λ (GeV)	0.2	0.4	0.4	0.6
μ_0 (GeV)	1.0	0.5	1.0	1.5
$\langle n_{\rm parton}\rangle$	5.9	10.8	8.6	7.3
$\langle n_g\rangle$	3.8	8.3	6.3	5.0
$\langle n_q + n_{\bar{q}}\rangle$	2.1	2.5	2.3	2.3
$\langle n_{\rm cluster}\rangle$	4.9	9.5	7.7	7.3
$\langle n_{\rm parton}\rangle$/cluster	1.2	1.1	1.1	1.0
$\langle M_{\rm cluster}\rangle$ (GeV)	1.08	0.68	1.09	1.54

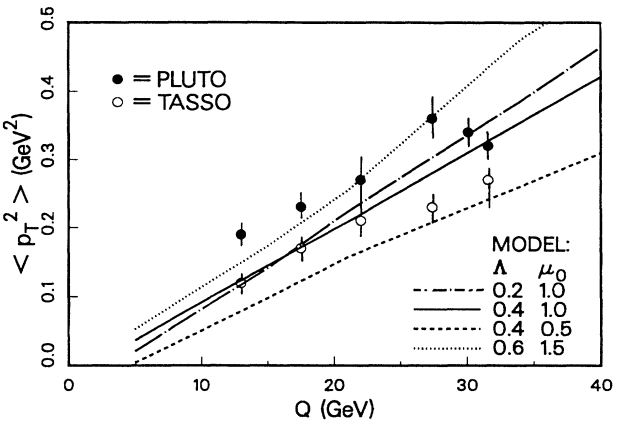

FIG. 8. Mean transverse momentum of charged particles in e^+e^- → hadrons, relative to the sphericity axis, as a function of center-of-mass energy Q. The data are from Refs. [56,57].

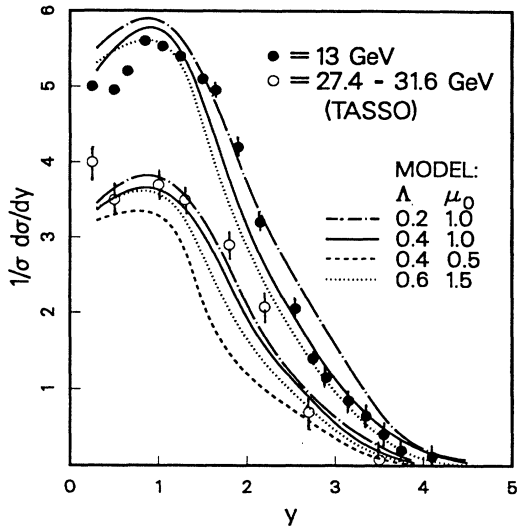

FIG. 9. Charged particle rapidity distribution in e^+e^--annihilation events at Q = 13 GeV and Q = 29 GeV. The experimental data are from Ref. [58]. Both the model results and the data are relative to the thrust axis.

μ_0. A choice leading to a high mass scale for color singlet clusters implies less perturbative parton production but a larger hadron multiplicity per cluster, and vice versa. Within a reasonable range, a particular choice of Λ and μ_0 amounts to shifting the scale that separates perturbative and nonperturbative descriptions and determines how much of the dynamics is attributed to each of the two regimes. The dependence on the fission threshold $M_{\rm fiss}$ is weak, because, as explained in Sec. III B 1, the anisotropic fission of massive clusters is a refinement that affects only a small fraction of clusters. In the following the fission threshold $M_{\rm fiss}$ is kept fixed at the reasonable value of 4 GeV throughout.

Figures 7–13 exhibit the effects of the choice of Λ and μ_0 for the four combinations (Λ, μ_0) = (0.2, 1), (0.4, 1), (0.4, 0.5), (0.6, 1.5) GeV and compare the resulting predictions for various observables in e^+e^- annihilation with experimental data. In Fig. 7 the $p_\perp$ distribution of the final charged hadrons with respect to the sphericity axis [54] is plotted for the two center-of-mass energies Q = 15 GeV and Q = 29 GeV, whereas Fig. 8 shows $\langle p_\perp^2 \rangle$ as a function of Q. The significance of the tail in the $p_\perp$ distribution and the magnitude of the resulting $\langle p_\perp^2 \rangle$ are governed by two effects [12]. First, the higher the in-

TABLE II. Dependence of various e^+e^- annihilation properties on the model parameters Λ, μ_0, and $M_{\rm fiss}$ at Q = 34 GeV.

Λ (GeV)	0.2	0.4	0.4	0.4	0.6	0.6	Experiment
μ_0 (GeV)	1.0	0.5	1.0	1.0	1.5	1.5	Ref. [65]
$M_{\rm fiss}$ (GeV)	4.0	4.0	∞	4.0	∞	4.0	
$\langle n_{\rm ch} \rangle$	11.7	15.6	12.5	13.5	12.3	12.9	13.6 ± 0.9
$\langle n_{\rm ch} \rangle / \langle n_{\rm hadron} \rangle$	0.58	0.57	0.58	0.57	0.59	0.58	–
$\langle n_{\pi^+} + n_{\pi^-} \rangle$	9.4	13.0	9.9	10.6	9.8	10.4	10.3 ± 0.4
$\langle n_{K^+} + n_{K^-} \rangle$	1.4	1.9	1.7	1.8	1.4	1.7	2.0 ± 0.2
$\langle n_p + n_{\bar{p}} \rangle$	0.8	0.6	0.6	0.7	0.8	0.8	0.8 ± 0.1
$\langle p_\parallel \rangle_{\rm sph}$ (GeV)	1.46	1.14	1.38	1.31	1.51	1.43	1.48 ± 0.11
$\langle p_\perp \rangle_{\rm sph}$ (GeV)	0.44	0.41	0.44	0.45	0.51	0.51	0.46 ± 0.11
$\langle p_\perp^2 \rangle_{\rm sph}$ (GeV^2)	0.39	0.26	0.31	0.35	0.47	0.48	0.32 ± 0.03
$\langle E \rangle_{\rm sph}$ (GeV)	1.66	1.34	1.57	1.52	1.72	1.66	–
$\langle S \rangle$	0.11	0.09	0.14	0.12	0.16	0.14	0.13 ± 0.04
$\langle T \rangle$	0.88	0.86	0.85	0.87	0.83	0.86	0.89 ± 0.02

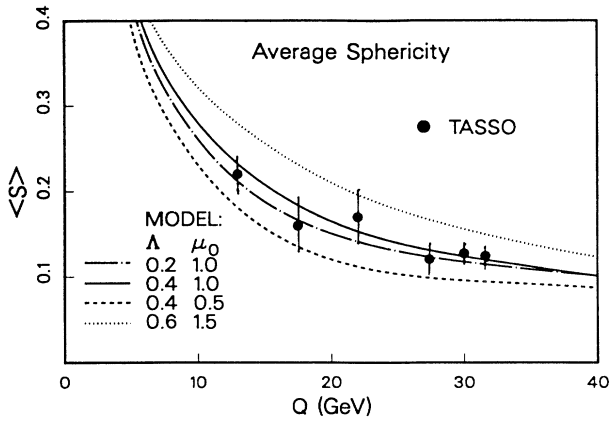

FIG. 10. $e^+e^- \rightarrow$ hadrons: average sphericity versus center-of-mass energy Q. The data are from Ref. [59].

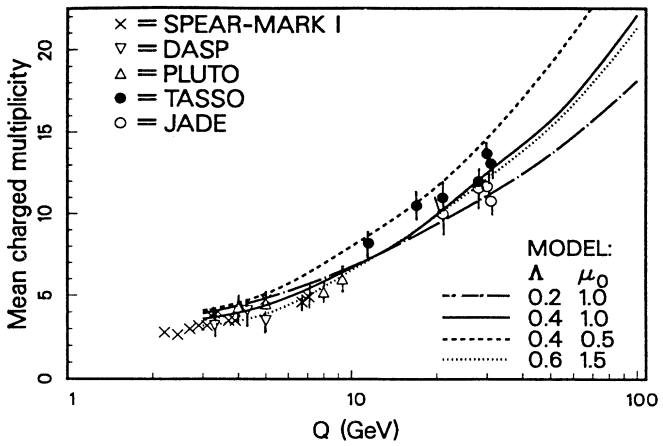

FIG. 12. Overall mean charged multiplicity in e^+e^- hadrons. The data are from Refs. [60–64].

variant mass of the individual cluster, the larger will be the transverse momentum generated in their decays into hadrons. Second, the larger Λ is, the higher is the probability for the emission of large transverse momentum gluons during the perturbative cascade evolution, which leads to a larger power-law tail in the partons' $p_\perp$ distribution and hence in the $p_\perp$ spectrum of the resulting hadrons. Thus, the largest $\langle p_\perp^2 \rangle$ is obtained with a large Λ (hence large α_s) and large μ_0 (hence large cluster masses). In accord with that observation is the effect of Λ and μ_0 on the rapidity (y) distributions of charged hadrons, which are shown in Fig. 9 for $Q = 13$ GeV and $Q = 29$ GeV, corresponding to the experimental data points. For both the model results and the data, the rapidities were computed with respect to the thrust axis [55]. The curves tend to shift towards smaller rapidities if either Λ and μ_0 are large, resulting in an increasing number of high mass clusters and large transverse momentum hadrons with small values of y, or for Λ and μ_0 small, yielding many low mass clusters whose decays result in a y distribution dominated by low momentum hadrons at small rapidities. It is interesting to note that the calculated rapidity distributions have a characteristic slight dip at zero rapidity, which is a reflection of the depletion of partons in the small rapidity region around $y = 0$ due to destructive interference of soft gluons in the perturbative branching processes in the cascade evolution. Figs. 10 and 11 show the average values of sphericity and of thrust as a function of Q, respectively. They reflect the energy dependence of the average produced transverse and longitudinal momentum. The curves again correspond to the model calculations for different parameter choices, whereas the data points are the corresponding experimental results.

The multiplicities of produced hadrons and the sensitivity of the model predictions to a variation of Λ and μ_0 are subjects of Figs. 12 and 13. In Fig. 12 the over-

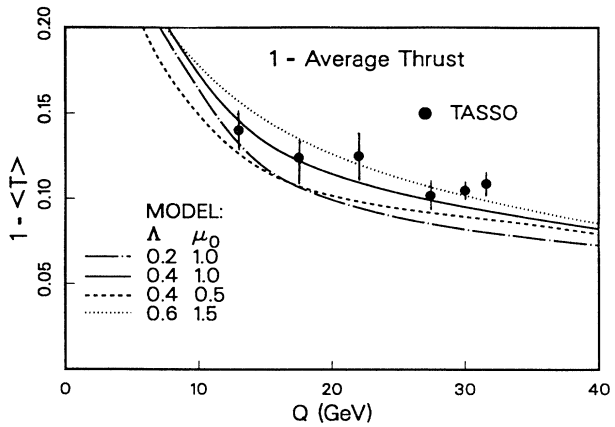

FIG. 11. $e^+e^- \rightarrow$ hadrons: average value of 1-thrust versus center-of-mass energy Q. The data are from Ref. [59].

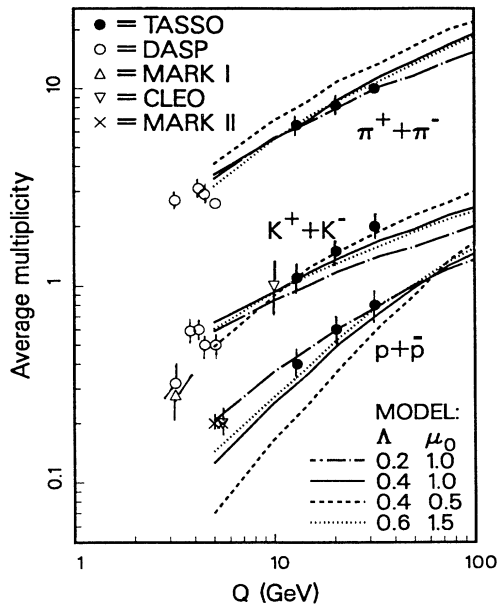

FIG. 13. $e^+e^- \rightarrow$ hadrons: Charged particle average multiplicities as function of center-of-mass energy Q. Data are from Ref. [65].

all multiplicity of final charged particles is shown as a function of Q, whereas Fig. 13 depicts the behavior of the average $\pi^+ + \pi^-$, $K^+ + K^-$, and $p + \bar{p}$ multiplicities with increasing center-of-mass energy. As expected from the previous discussion, a parameter combination with Λ small and μ_0 small results in a larger overall multiplicity and a stronger increase with Q than one with both Λ and μ_0 being large. Also, pion production dominates in this case, because kaon and baryon production is suppressed by the larger K and p masses and a larger number of π than K is produced in the decays of low-lying meson resonances. Note that the measured approximate constancy of the total charged hadron multiplicity over the range $1.5 \leq Q \leq 4$ GeV in Fig. 12 supports the assumption that clusters with masses in this range directly convert into pairs of light mesons or baryons without cascading through clusters of intermediate mass, i.e., without cluster fission. Accordingly, the fission threshold of $M_{\text{fiss}} = 4$ GeV, as employed in the calculations, seems to be a reasonable choice.

Finally, in Fig. 14 the dependence on Λ and μ_0 of the multiplicity of final partons at the end of the cascade development is shown, and Fig. 15 shows the resulting ratio of the charged hadron multiplicity (which is proportional to the total hadron multiplicity—from Table II, $\langle n_{\text{ch}} \rangle / \langle n_{\text{hadron}} \rangle \simeq 0.6$) to the parton multiplicity. The relation between parton and hadron multiplicities is interesting to investigate, particularly as Fig. 5 suggests that the mass spectrum of color singlet clusters is independent of the center-of-mass energy, in agreement with analytical predictions [9,10]. This implies that parton and hadron multiplicities should be proportional to each other at asymptotic energies. Figure 15 indicates such a behavior as it exhibits the approach of the charged hadron to parton ratio to a constant value for each of the four parameter combinations. The absolute value of this ratio clearly depends on the choice of Λ and μ_0, but

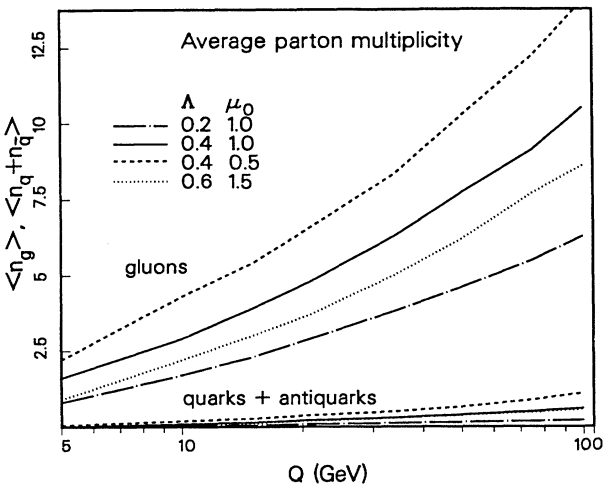

FIG. 14. Average multiplicities of quarks and gluons produced in e^+e^- annihilation. Only secondary final state partons are counted, i.e., the cascade initiating q and $\bar{q}$ created by the virtual photon are not accounted for.

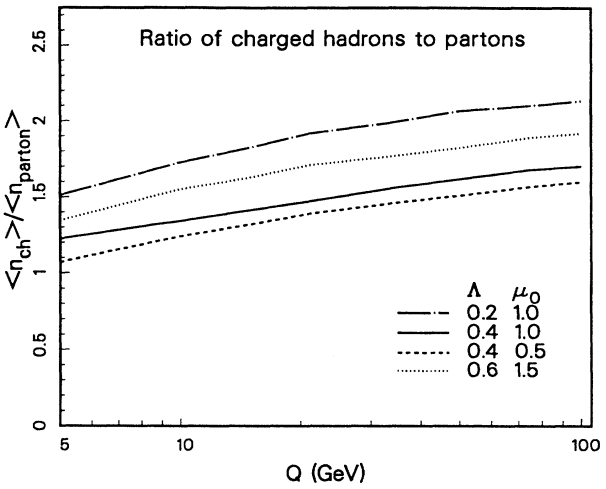

FIG. 15. Ratio of mean charged multiplicity to parton multiplicity in $e^+e^- \rightarrow$ hadrons.

the amount of increase with energy is roughly the same for the different parameter choices. In all four cases the approach to a specific asymptotic value proceeds almost identically. Furthermore one observes that the ratios increase rather slowly over the range from 5 to 100 GeV, implying only a moderate energy dependence already at realistic center-of-mass energies.

In conclusion, the investigation of the parameter dependence of the parton cascade–cluster hadronization model shows that the choice

$$\Lambda = 0.4 \text{ GeV}, \quad \mu_0 = 1 \text{ GeV}, \quad M_{\text{fiss}} = 4 \text{ GeV} \tag{41}$$

yields the best overall agreement with the experimental e^+e^- data. The measured momentum spectra as well as the particle multiplicities are most accurately reproduced with this particular parameter combination. Therefore, in the following these values will be used throughout and will be considered to be universally the same for $p\bar{p}$ and AA collisions which are the subject of the following Secs. IV B and IV C.

B. Particle production in $p\bar{p}$ collisions at $\sqrt{s} = 200$–1800 GeV

With the fundamental scale Λ and the invariant mass cutoff μ_0 fixed, the model description of the perturbative and hadronization stages is unambiguously defined. Since the assumption of the hadronization process as a local phenomenon implies that the conversion of partons into hadrons must be universal and independent of the specific reaction, the combined parton cascade–cluster fragmentation approach should work equally as well for hadronic and nuclear reactions as in the previous case of e^+e^- annihilation. However, when proceeding to hadron-hadron or nucleus-nucleus collisions additional physics aspects arise due to the presence of initial state partons; for example, the effects of multiple interactions among the quanta, the role of soft QCD, and collective

phenomena. As outlined in Secs. II A and II B, the ansatz for the initial parton distribution and the kinetic formulation of the parton cascade development takes into account a number of these aspects in a phenomenological manner and supplements the primary role of the perturbative QCD description of the dynamics. Although the hadronization process factorizes and is locally independent of the preceding evolution, the specific space-time structure of the final parton configuration determines the initial conditions for the formation of hadrons and should therefore be reflected in the observable final particle spectra. Before focusing on heavy ion reactions, it is useful to test the model as a whole in applying it to high energy $p\bar{p}$ collisions which have been studied experimentally as well as theoretically in great detail. I will discuss some important features of particle production in $p\bar{p}$ collisions at the collider energies $\sqrt{s}$ = 200, 546, 900, 1800 GeV, where many high statistics data have been collected by the collaborations UA1, UA2, and UA5 at CERN and the CDF collaboration at the Tevatron. The data that I will consider here have been discussed before by others [17,66–68]. In particular, Sjöstrand and van Zjil [67] and recently Wang and Guylassy [68] have studied in detail the important role of perturbative QCD semihard parton interactions and minijet production in this energy range and tried to disentangle it from the underlying soft physics.

The following results for $p\bar{p}$ collisions were obtained by (i) generating the initial parton distributions in the incoming p and $\bar{p}$ as explained in Sec. II A with a randomly chosen impact parameter b according to the phase-space d^2b and $0 \leq b \leq b_{\max} \simeq \sqrt{\sigma_{p\bar{p}}(s)/\pi}$, where $\sigma_{p\bar{p}}(s)$ is the measured inelastic $p\bar{p}$ cross section [51]; (ii) evolving the parton distributions in phase space along the parton cascade development, described in Sec. II B, until the interactions among the partons cease (about 1 fm/c after the first hadronic contact); and (iii) hadronizing the final partons with the cluster fragmentation scheme of Secs. III A and III B. Unless noted otherwise, all results refer to averages over the impact parameter b. Tables III–V summarize some average properties of $p\bar{p}$ collision events generated in this fashion for different collider energies. In Table III the dependence of the relative contributions of the various parton interaction processes on the beam energy $\sqrt{s}$ is exhibited, whereas Table IV demonstrates the increase with $\sqrt{s}$ of the total number of partons in the reactions. The initial primary partons arise from resolving the incoming p and $\bar{p}$ into their substructure and the final partons before cluster formation are distinguished in primary and secondary partons. Table V gives the mean numbers of some of the resulting hadron species and their average transverse momenta at $\sqrt{s}$ = 546 GeV, as compared to the experimental data [69,70]. The general agreement of the model results with the measured data is decent.

Figures 16(a,b) show the invariant inclusive cross-section as a function of $p_\perp$ from the calculation for the final state parton configuration before hadronization and for the resulting hadrons, respectively. Comparing the two plots, one sees that the shape of the final hadron distribution in Fig. 16(b) is essentially predetermined by the $p_\perp$ distribution at the parton level in Fig. 16(a). The additional "intrinsic transverse momentum" generated in the hadronization is determined by the average energy release in cluster decays (and in the subsequent decay chain of produced hadron resonances). At large $p_\perp$ ($\geq$ 2 GeV), the curves reflect the onset of the truly perturbative QCD contribution by a characteristic power law tail, instead of

TABLE III. Dynamical quantities and mean number of parton interactions in simulated $p\bar{p}$ collisions at $\sqrt{s}$ = 200–1800 GeV. The values of Q_0 are obtained from accumulated statistics according to Eq. (1), whereas $p_{\perp\text{cut}}$, μ_0, and $b_{\max}$ are input values.

Quantity	$\sqrt{s}$ = 200 GeV	$\sqrt{s}$ = 546 GeV	$\sqrt{s}$ = 900 GeV	$\sqrt{s}$ = 1800 GeV
Q_0 (GeV)	1.88	2.65	3.42	4.84
$p_{\perp\text{cut}}$ (GeV)	1.50	1.70	2.55	3.45
μ_0 (GeV)	1	1	1	1
$b_{\max}$ (fm)	1.30	1.40	1.55	1.95
$\langle n_{2\to2}^{(\text{hard})} \rangle$	2.58	5.35	7.68	9.04
$\langle n_{2\to2}^{(\text{soft})} \rangle$	0.78	1.03	1.86	3.29
$\langle n_{2\to2}^{(\text{prim.coll.})} \rangle$	2.42	3.96	4.94	5.88
$\langle n_{2\to1} \rangle$	0.07	0.15	0.29	0.58
$\langle n_{1\to2}^{(\text{timelike})} \rangle$	3.58	6.85	15.61	24.27
$\langle n_{1\to2}^{(\text{spacelike})} \rangle$	0.030	0.029	0.021	0.008
% events with no parton scattering	0.31	0.21	0.16	0.07

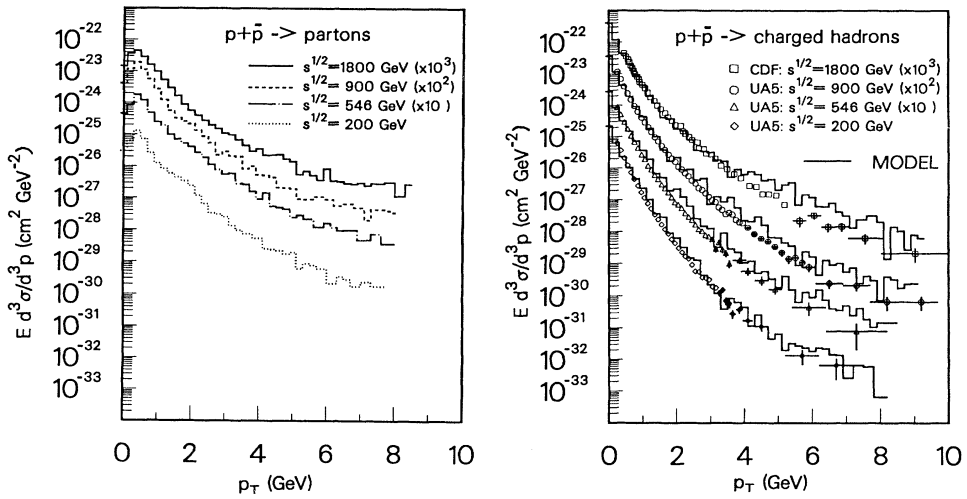

FIG. 16. Invariant inclusive cross sections of (a) partons and (b) charged hadrons in $p\bar{p}$ collisions at $\sqrt{s}$ = 200–1800 GeV. The histograms are model results and the data are from Refs. [71,72]. Both the calculation and experimental data refer to the (pseudo)rapidity regions $|\eta| < 2.5$ for $\sqrt{s}$ = 200, 546, and 900 GeV, and $|\eta| < 1$ for $\sqrt{s}$ = 1800 GeV.

being of exponential form. At low $p_\perp$ ($\leq$ 2 GeV), soft physics is dominant, which in the model is accounted for by the phenomenological soft parton-parton scatterings with $p_\perp < p_{\perp\text{cut}}$ (8), but multiple semihard and hard parton collisions with $p_\perp > p_{\perp\text{cut}}$ and the production of additional transverse momentum in associated parton branchings contribute increasingly with $\sqrt{s}$ to this low $p_\perp$ background as well. Here the $p_{\perp\text{cut}}$ scale, dividing soft from perturbative QCD interactions, is of essential importance to give a satisfactory reproduction of the data [71,72] over the full $p_\perp$ range. In fact the values for $p_{\perp\text{cut}}$ implied by the formula (8) had to be slightly adjusted to

TABLE IV. Average multiplicities of partons and resulting hadrons in simulated $p\bar{p}$ collisions at $\sqrt{s}$ = 200–1800 GeV. The partons are distinguished in primary and secondary quanta. The initial parton distributions consist only of primary quanta whereas the final parton configuration shows both the numbers of remaining spectator partons (prim.) and the multiplicities of interacted or produced partons (sec.). The hadron multiplicities and their average $p_\perp$ result from the cluster hadronization of these final partons.

Quantity	$\sqrt{s}$ = 200 GeV		$\sqrt{s}$ = 546 GeV		$\sqrt{s}$ = 900 GeV		$\sqrt{s}$ = 1800 GeV	
Initial partons	prim.	sec.	prim.	sec.	prim.	sec.	prim.	sec.
$\langle n_{\text{parton}}\rangle$	59.11	–	76.10	–	93.70	–	103.09	–
$\langle n_g\rangle$	43.01	–	56.59	–	69.29	–	76.23	–
$\langle n_u + n_{\bar{u}}\rangle$	7.28	–	8.34	–	9.32	–	10.23	–
$\langle n_d + n_{\bar{d}}\rangle$	5.00	–	6.04	–	7.46	–	8.00	–
$\langle n_s + n_{\bar{s}}\rangle$	3.04	–	3.97	–	5.47	–	5.45	–
$\langle n_c + n_{\bar{c}}\rangle$	0.78	–	1.16	–	2.16	–	3.02	–
Final partons	prim.	sec.	prim.	sec.	prim.	sec.	prim.	sec.
$\langle n_{\text{parton}}\rangle$	56.02	5.52	70.40	10.97	86.88	21.91	93.43	31.60
$\langle n_g\rangle$	40.75	4.41	52.32	8.84	63.29	18.89	68.65	26.58
$\langle n_u + n_{\bar{u}}\rangle$	6.88	0.46	7.38	1.18	8.83	1.41	9.45	1.73
$\langle n_d + n_{\bar{d}}\rangle$	4.74	0.38	5.80	0.50	7.29	0.75	7.50	1.50
$\langle n_s + n_{\bar{s}}\rangle$	2.92	0.20	3.83	0.34	5.42	0.63	5.08	1.28
$\langle n_c + n_{\bar{c}}\rangle$	0.73	0.07	1.07	0.11	2.05	0.23	2.75	0.51
Final hadrons								
$\langle n_{\text{ch}}\rangle$	20.3		29.9		35.1		42.7	
$\langle n_{\text{ch}}\rangle/\langle n_{\text{hadron}}\rangle$	0.57		0.57		0.58		0.59	
$\langle p_{\perp\text{ ch}}\rangle$ (GeV)	0.39		0.43		0.48		0.51	
$\langle p^2_{\perp\text{ ch}}\rangle$ (GeV^2)	0.31		0.35		0.47		0.61	

TABLE V. Model results for minimum bias event properties in $p\bar{p}$ collisions at $\sqrt{s} = 546$ GeV in comparison with experimental data from UA5 [69] (except for $\langle p_{\perp p} \rangle$ which is from UA2 [70]).

Quantity	Model	UA5 Ref. [69]
$\langle n_{\rm ch} \rangle$	29.9	29.4 ± 0.3
$\langle n_{\pi^+} + n_{\pi^-} \rangle$	22.3	23.9 ± 0.4
$\langle n_\gamma \rangle$	27.8	33.0 ± 3.0
$\langle n_{K^0} + n_{\bar{K}^0} \rangle$	2.78	2.24 ± 0.16
$\langle n_p + n_{\bar{p}} \rangle$	2.51	2.45 ± 0.15
$\langle n_\Lambda + n_{\bar{\Lambda}} \rangle$	0.83	0.53 ± 0.11
$\langle n_{\Xi^-} + n_{\bar{\Xi}^+} \rangle$	0.16	0.10 ± 0.03
$\langle p_{\perp \rm ch} \rangle$	0.43	0.42 ± 0.02
$\langle p_{\perp \pi^\pm} \rangle$	0.36	0.39 ± 0.03
$\langle p_{\perp \gamma} \rangle$	0.18	0.20 ± 0.02
$\langle p_{\perp K^0} \rangle$	0.61	0.57 ± 0.03
$\langle p_{\perp p} \rangle$	0.74	0.66 ± 0.05

the ones given in Table III in order to achieve the shown agreement with the data.

In Figs. 17(a,b) the pseudorapidity distributions of the final state partons and the charged hadrons, respectively, are shown, in correspondence to Figs. 16(a,b) (note that for the partons $y \simeq \eta$, even for very small rapidities). For comparison, also the experimental results [73,74] are plotted in Fig. 17(b). Figure 17(a) clearly exhibits a depletion of partons around zero rapidity which is, as mentioned in Sec. III A (Fig. 9), a consequence of the destructive interference of soft gluons in the cascades. Again one observes from the similarity of the parton and hadron spectra that the hadronization does not wash out the partons' rapidity distributions and that the latter manifests itself in the observable hadron spectra. Figure 17(b) demonstrates a good agreement of the calculated histograms with the collider data. The model results reproduce both the overall widening of the distributions and the increase of the central rapidity density with the beam energy. Note that the calculations as well as the data in Fig. 17(b) refer to "nonsingle diffractive" events [75] which are in the energy range considered here mostly true "nondiffractive" events (except for a small fraction of "double diffractive events") [38].

Whereas the increase of the overall width of the rapidity distributions proportional to $\sqrt{s}$ is essentially the consequence of a larger energy and longitudinal momentum brought into the reactions, the increase of the central rapidity density around $\eta = 0$ is totally due to the growing number of parton-parton collisions and the multiplicity increase of partons produced in the associated cascades (cf. Table IV). This correlation between central rapidity density and increasing minijet production was already found in the similar studies of Refs. [67,68], which led to the prediction of a nonlinear growth $(d\sigma/d\eta)_{\eta=0} \propto \ln(\sqrt{s})$ [68].

The effects of the increasing number of parton cascades due to multiple parton collisions is also clearly reflected when analyzing the multiplicity distributions of final charged hadrons. Figure 18 shows the total charged particle multiplicity distributions from the calculations and the corresponding data [69,76] at $\sqrt{s} = 200$, 546, and 900 GeV. The model results (full histograms) decently reproduce the systematic widening of the measured distributions with increasing collider energy. It is very illuminating to see how the contributions from events with $k = 0$, 1, 2, and ≥ 3 parton-parton collisions (indicated by the patterned curves) add up to give the total distributions: the low multiplicity region is dominated by events with no parton scatterings above $p_{\perp \rm cut}$, whereas the high multiplicity tail is due to events with several interactions. Furthermore, the average charged multiplicity $\langle n_{\rm ch} \rangle$ also increases with the mean number of interactions, as is obvious from Table IV and from the shift of the peak in the plots of Fig. 18. However each additional interaction gives a smaller contribution than the preceding one, so that there seems to be a saturation. These features have independently been studied within

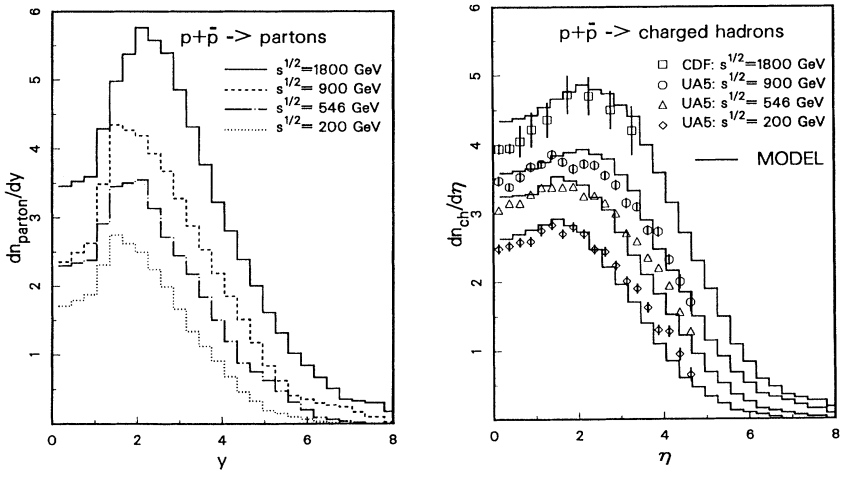

FIG. 17. (a) Rapidity spectra of partons and (b) corresponding pseudorapidity distributions of charged hadrons in $p\bar{p}$ collisions at $\sqrt{s} = 200$–1800 GeV. The model results are shown as histograms and the data points are from Refs. [73,74].

perturbative QCD before [67,68] with similar results as here. The model independence of the predictions and the agreement with the measured distributions provide strong support for the evidence of multiple parton interactions and manifests the important role of semihard perturbative QCD for the event structure.

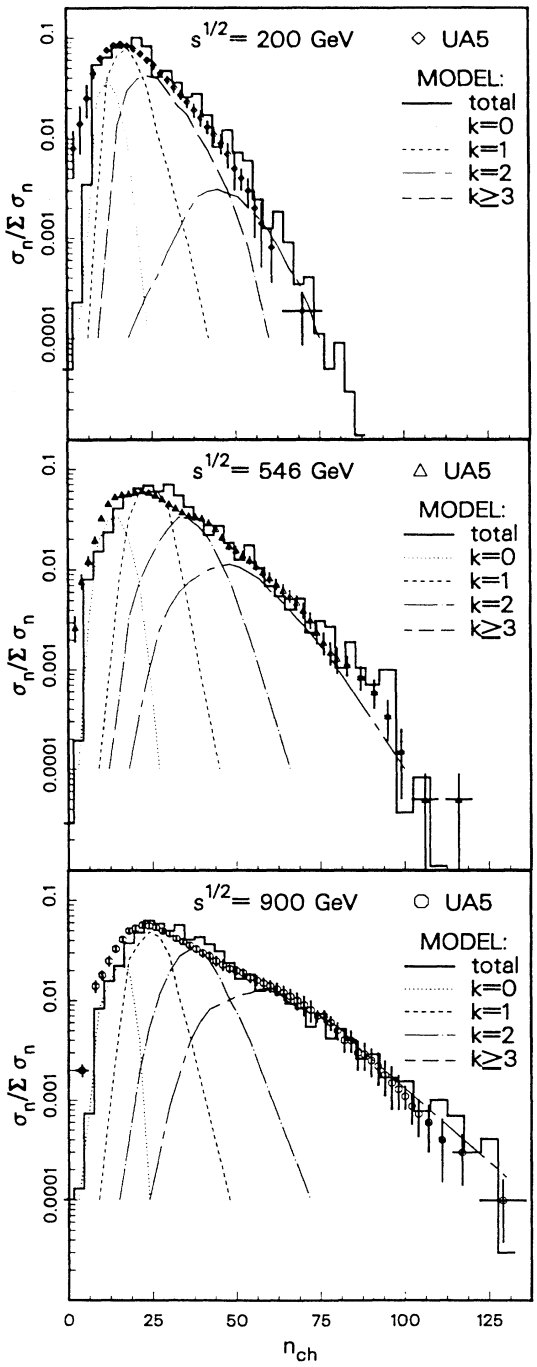

FIG. 18. Charged particle multiplicity distributions in $p\bar{p}$ collisions at $\sqrt{s}$ = 200, 546, and 900 GeV. The data points are from Refs. [75,76]. The histograms are the calculated distributions. The various patterned curves result from separating the contributions from events with $k = 0, 1, 2$, and ≥ 3 parton-parton interactions.

In the calculations presented here, the number of parton collisions and consequently the multiplicities of partons produced in the initiated cascades is strongly correlated with the impact parameter b of the beam particles p and $\bar{p}$. Due to the proportionality between parton and hadron multiplicity, pointed out in Sec. III A and Fig. 15, the shape of charged particle multiplicity distributions is a direct consequence of the distribution of parton interactions with the $p\bar{p}$ impact parameter. Figure 19 displays the model results for the number of parton-parton collisions, the multiplicities of partons produced in the cascades initiated by these collisions and the final charged particle multiplicities, respectively, as a function of impact parameter for the different beam energies. In order to achieve the shown agreement with the measured distributions, the maximum impact parameter $b_{\max}$ was fine tuned around the value $\sqrt{\sigma_{p\bar{p}}(s)/\pi}$ which results in the values listed in Table III. It is obvious that the largest

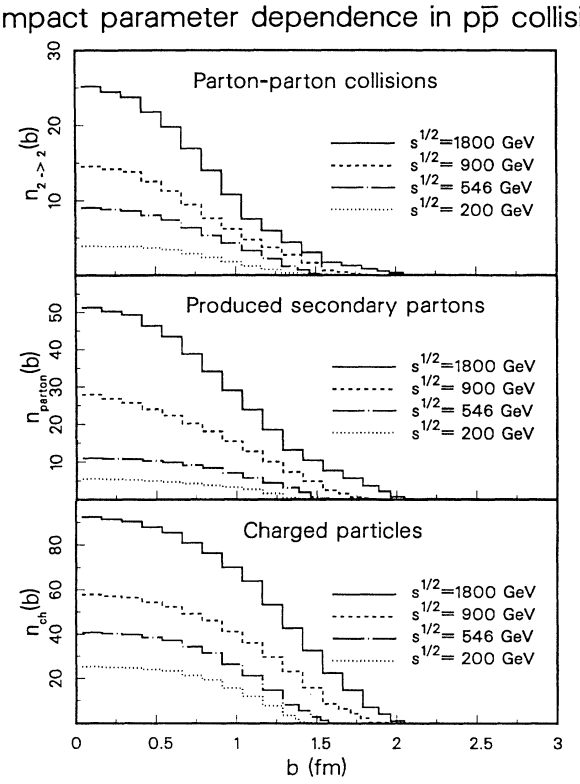

FIG. 19. Impact parameter dependence of (a) the number of parton-parton collisions, (b) the number of partons produced in the associated cascades, and (c) the number of final charged hadrons in $p\bar{p}$ collisions at $\sqrt{s}$ = 200–1800 GeV. The $p\bar{p}$ impact parameter was chosen according to the phase-space d^2b with $0 \leq b \leq b_{\max}$, where the values for $b_{\max}$ are given in Table III.

number of interactions occurs in the mean in central collisions, resulting in the largest multiplicity of partons and subsequently hadrons. The more peripheral the reactions are, the more probable are events with only one or no parton-parton collision, which yields the decreasing tail as $b \to b_{\max}$. As one proceeds to higher collider energies the curves become steeper and more peaked at $b = 0$. This is consistent with the increasing high multiplicity tails in Fig. 18 which obviously are mainly due to central collisions events for which the multiplicity enhancement is the strongest.

C. Central Au + Au collisions at RHIC and LHC

Nucleus-nucleus collisions at collider energies, in particular those involving heavy ions, are expected to exhibit novel effects in the dynamical evolution [5] and multiparticle production [3]. It is these reactions for which the parton cascade model provides a special opportunity to study the relevance of new physical features, not visible or significant in hadronic collisions. In the following I will present simulation results of Au + Au collisions at zero impact parameter at $\sqrt{s} = 200A$ GeV and $\sqrt{s} = 6300A$ GeV, corresponding to the collider energies of RHIC and LHC, respectively. The time evolution of the partons' phase-space distributions was followed from the moment of nuclear touch, as described in Sec. II. The analysis of Ref. [6] showed that after about 3 fm/c, in the central collision region an equilibrated quark-gluon plasma state with a volume $\simeq 100$ fm^{-3} is established, while the majority of spectator partons form two beam fronts which quickly recede from the central region. It is clear that the conversion of a quark-gluon plasma into hadrons is a much more complicated process than the hadronization of final state partons in dilute systems as, e.g., in hadron-hadron collisions. The transition is expected to involve a rather long time scale ($\simeq 10$ fm/c) and might proceed first as an expansion and cooling of the plasma and then through a mixed parton-hadron phase to a purely hadronic phase. Several models have been proposed to describe the hadronization of quark-gluon plasmas (see Ref. [77] and references therein). Instead of attempting to model a detailed space-time description of the parton-hadron transition, here the following simple prescription is employed: The whole system of partons is evolved in space-time for about 5 fm/c after the perturbative cascade development has ceased, with the partons streaming freely apart along classical trajectories. At that time (corresponding to $\simeq$ 8–10 fm/c after the first nuclear contact) even the partons in the densely populated central region have separated sufficiently to be considered as distinct, noninterfering quanta. The system of these final state partons is then hadronized at once, according to the cluster hadronization scheme of Sec. III.

As mentioned in Sec. II, the model incorporates a number of phenomena associated with the partons' space-time development in nuclear collisions, which in Ref. [5] have been shown to drastically alter the microscopic dynamics of the partons. The question is, how clearly these effects are reflected in the final hadron spectra and if it is possible to disentangle the significance of the different phenomena. In the following I will therefore consider five different evolution scenarios for the parton distributions. Not only do they give rather distinct results, but also exhibit a clear impact of nuclear effects in the charged particle spectra when compared with pp collisions at corresponding energies. The evolution schemes are as follows (see Ref. [5] for details):

(a) *"Naive evolution"*: Parton shadowing in the initial parton distributions is neglected. Parton scatterings occur instantaneously without time delay. Associated cascades of successive parton branchings happen immediately at the same space-time point as the scattering, i.e., with zero formation time for radiative emissions. Absorptive processes and soft gluon interference are switched off.

(b) *Nuclear shadowing*: As (a), but now the initial parton distributions are modified to account for nuclear shadowing effects as explained in Sec. II A.

(c) *Parton fusion and absorption*: As (b), but in addition the time scale for each individual parton-parton collision is taken into account. Parton fusion and absorptive processes compete with the emission of partons in the cascades.

(d) *Landau-Pomeranchuk effect*: As (c), but furthermore, successive parton branchings in the cascade evolution are delayed according to the characteristic formation time for gluon emissions.

(e) *Soft gluon interference*: As (d), but moreover, the destructive interference of soft gluons decreases the available phase-space for low energetic gluon bremsstrahlung.

TABLE VI. Model results for dynamical quantities and mean number of parton interactions in central Au + Au collisions at $\sqrt{s} = 200A$ GeV and $\sqrt{s} = 6300A$ GeV. The values of Q_0 are obtained from accumulated statistics according to Eq. (1), whereas $p_{\perp\text{cut}}$ and μ_0 are input values.

Quantity	$\sqrt{s} = 200A$ GeV (RHIC)	$\sqrt{s} = 6300A$ GeV (LHC)
Q_0 (GeV)	2.28	5.23
$p_{\perp\text{cut}}$ (GeV)	1.55	3.95
μ_0 (GeV)	1	1
$\langle n_{2\to2}^{(\text{hard})} \rangle$	11026	37980
$\langle n_{2\to2}^{(\text{soft})} \rangle$	2855	10345
$\langle n_{2\to2}^{(\text{prim.coll.})} \rangle$	4674	9249
$\langle n_{2\to1} \rangle$	860	7266
$\langle n_{1\to2}^{(\text{timelike})} \rangle$	7451	24120
$\langle n_{1\to2}^{(\text{spacelike})} \rangle$	143	278

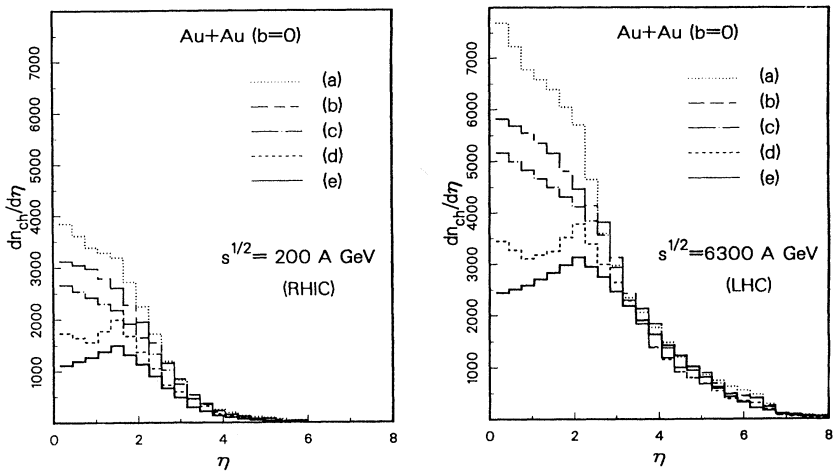

FIG. 20. The model predictions (solid histogram) for the pseudorapidity distributions of charged particles in central Au + Au collisions at $\sqrt{s} = 200A$ GeV (left) and $\sqrt{s} = 6300A$ GeV (right). The various histograms show the characteristics of the space-time evolution schemes (a)–(e) defined in Sec. IV C: (a) "naive" evolution (dotted), (b) nuclear shadowing (long dashed), (c) parton fusion and absorption (dashed dotted), (d) Landau-Pomeranchuk effect (short dashed), and (e) soft gluon interference (solid). Note that case (e) is the full calculation including all these effects.

The Tables VI and VII summarize some average properties of simulated Au + Au events for the evolution scheme (e) which includes all these effects. Table VI lists the mean numbers of the various parton interactions (cf. Table III) and Table VII gives the average numbers of initial and final partons as well as the resulting charged hadron multiplicities (cf. Table IV).

To illustrate the new physics associated with the effects in (a)–(e), I will focus here on the two simplest observables: the pseudorapidity and the transverse momentum spectra of final charged hadrons. Figures 20 and 21, show, respectively, the charged particle distributions in η and $p_\perp$, calculated for central Au + Au collisions with $\sqrt{s} = 200A$ GeV and $\sqrt{s} = 6300A$ GeV. The var-

TABLE VII. Average multiplicities of partons and resulting hadrons in central Au + Au collisions at $\sqrt{s} = 200A$ GeV and $\sqrt{s} = 6300A$ GeV as calculated with the space-time evolution scheme (e) defined in Sec. IV C. The partons are distinguished in primary and secondary quanta. The multiplicities of the initial partons were obtained from the nuclear structure functions and reflect the flavor composition of the incoming nuclei. The mean number of final partons refers to the parton distributions just before hadronization. The hadron multiplicities and their average $p_\perp$ result from the cluster hadronization of these final state parton configurations.

Quantity	$\sqrt{s} = 200A$ GeV (RHIC)		$\sqrt{s} = 6300A$ GeV (LHC)	
Initial partons	prim.	sec.	prim.	sec.
$\langle n_{\text{parton}} \rangle$	11821	–	20657	–
$\langle n_g \rangle$	8471	–	14825	–
$\langle n_u + n_{\bar{u}} \rangle$	1320	–	2284	–
$\langle n_d + n_{\bar{d}} \rangle$	1214	–	2112	–
$\langle n_s + n_{\bar{s}} \rangle$	666	–	1172	–
$\langle n_c + n_{\bar{c}} \rangle$	150	–	264	–
Final partons	prim.	sec.	prim.	sec.
$\langle n_{\text{parton}} \rangle$	5687	13638	7590	42454
$\langle n_g \rangle$	4165	10648	5214	33121
$\langle n_u + n_{\bar{u}} \rangle$	566	1146	910	3554
$\langle n_d + n_{\bar{d}} \rangle$	506	1064	822	3318
$\langle n_s + n_{\bar{s}} \rangle$	394	614	524	1930
$\langle n_c + n_{\bar{c}} \rangle$	56	166	120	532
Final hadrons				
$\langle n_{\text{ch}} \rangle$	6660		21420	
$\langle n_{\text{ch}} \rangle / \langle n_{\text{hadron}} \rangle$	0.58		0.60	
$\langle p_{\perp\, ch} \rangle$ (GeV)	0.39		0.54	

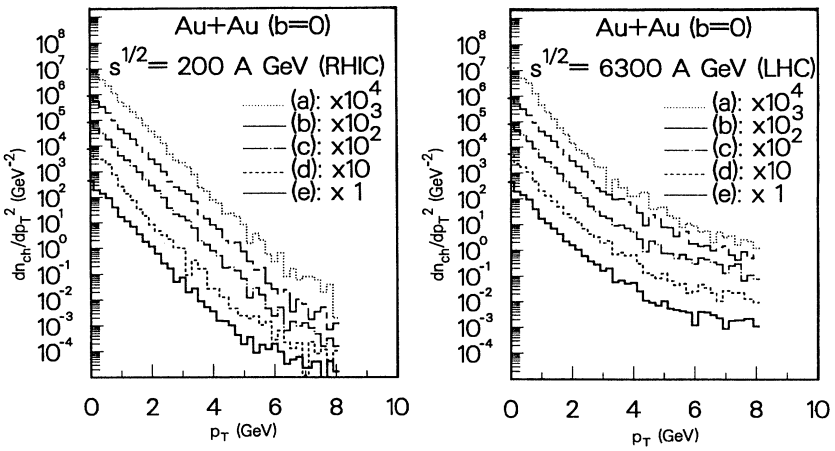

FIG. 21. The model predictions (solid histogram) for the transverse momentum distributions of charged particles in central Au + Au collisions at $\sqrt{s} = 200A$ GeV (left) and $\sqrt{s} = 6300A$ GeV (right). As in Fig. 19 the different histograms refer to the space-time evolution schemes (a)–(e) defined in Sec. IV C (for better presentation the distributions have been multiplied by powers of 10): (a) "naive" evolution (dotted), (b) nuclear shadowing (long dashed), (c) parton fusion and absorption (dashed dotted), (d) Landau-Pomeranchuk effect (short dashed), and (e) soft gluon interference (solid). Note that case (e) is the full calculation including all these effects.

ious curves (a)–(e) display the characteristics of the different evolution scenarios. As can be seen from Fig. 20, the particle density in the central rapidity region is reduced successively from the "naive" calculation [case (a)] to the default result [case (e)] by more than a factor of 3. For both collider energies the behavior is roughly the same, although the impact of nuclear shadowing [curve (b)] and the Landau-Pomeranchuk effect [curve (d)] seem to become more prominent at $\sqrt{s} = 6300A$ GeV. Obviously the drastic reduction of the charged particle yield is most significant at $\eta \approx 0$, because the inclusion of delayed gluon emission associated with the Landau-Pomeranchuk effect [case (d)] and soft gluon interference [case (e)] leads to a specific depletion of softer partons which is reflected by the dip appearing in the range $|\eta| \leq 1$. Although clearly mirrored in the hadron distributions, both these effects originate from the parton level: First, soft gluon radiation takes a longer formation time than the emission of harder gluons, so that it is suppressed by subsequent parton scatterings before it actually can occur. Second, the destructive interference of soft gluon emission amplitudes yields a further suppression of low energy quanta. Whereas the latter effect is a general property of QCD, independent of the reaction (cf. Figs. 9 and 17), the Landau-Pomeranchuk effect associated with the finite formation time of gluon radiation is certainly a novel nuclear phenomenon which not visible in, e.g., pp collisions, because there the phase-space density of partons is too low. For the total integrated charged particle yield the reduction from (a) to (e) is less dramatic than for the central rapidity density, but is still very large: from $\simeq$ 17000 to $\simeq$ 6600 ($\sqrt{s} = 200A$ GeV) and from $\simeq$ 42500 to $\simeq$ 21500 ($\sqrt{s} = 6300A$ GeV).

Comparing the η spectra for RHIC [Fig. 20(a)] and LHC [Fig. 20(b)] one sees that the central density only doubles [from $\simeq$ 1200 to $\simeq$ 2500 in case (e)] when the collider energy is increased by about a factor of 30. However, the total charged multiplicity grows from $\simeq$ 6600 to $\simeq$ 21500 from RHIC to LHS, i.e., by more than a factor of 3, because not only the height but also the width of the spectra increases.

Turning to the transverse momentum distributions of charged particles shown in Fig. 21, one notices that the curves corresponding to the evolution schemes (a)–(e) are hardly distinguishable in their shape (note that the curves have been multiplied by factors 10^k, $k = 0 - 4$, for better presentation). The slope is roughly the same for all five curves, at least for moderate $p_\perp \leq 3 - 4$ GeV. However, in the region $p_\perp \geq 6$ GeV the spectra appear to become slightly harder when comparing the curves from (a) to (e), in that this high $p_\perp$ domain becomes more populated. On the other hand, the comparison of the $p_\perp$ distributions for RHIC [Fig. 21(a)] and LHC [Fig. 21(b)] exhibits some interesting features: Aside from the already mentioned tripling of the total charged multiplicity, most prominent is the clear outgrowth of a power law tail for $p_\perp \geq 4$ GeV which is characteristic for the onset of QCD jet production. At RHIC ($\sqrt{s} = 200A$ GeV) this high $p_\perp$ tail is just beginning to develop, but is almost invisible. At both energies, the low and moderate $p_\perp$ region ≤ 4 GeV is characterized by an approximate exponential distribution $\sim \exp(-p_\perp/p_0)$ with $p_0 \simeq 0.35$ GeV ($\sqrt{s} = 200A$ GeV) and $p_0 \simeq 0.39$ GeV ($\sqrt{s} = 6300A$ GeV). The average $p_\perp$, however, increases more strongly (cf. Table VII) because of the significant $p_\perp$ contribution at LHC, namely from $\langle p_\perp \rangle \simeq 0.39$ GeV ($\sqrt{s} = 200A$ GeV) to $\langle p_\perp \rangle \simeq 0.54$ GeV ($\sqrt{s} = 6300A$ GeV) .

Finally, it is instructive to compare the charged particle η and $p_\perp$ spectra in Au + Au collisions of Figs. 20 and 21 with the momentum distributions in $p + \bar{p}$ collisions shown in Figs. 17(b) and 16(b), at the corresponding energies per nucleon. In $p + \bar{p}$ ($p + p$) collisions the typical central rapidity densities are $\simeq$ 2.4 for $\sqrt{s} = 200$ GeV and $\simeq$ 5.3 for $\sqrt{s} = 6300$ GeV [68], whereas for Au + Au at $b = 0$ fm Fig. 20 [case (e)] shows central densities of $\simeq$ 1200 ($\sqrt{s} = 200A$ GeV) and $\simeq$ 2500 ($\sqrt{s} = 6300A$ GeV). Hence, even for the evolution scheme (e) with the lowest multiplicities, one has $dn_{\rm ch}^{AA}/d\eta|_{\eta=0} \simeq 2.4\ A\ dn_{\rm ch}^{pp}/d\eta|_{\eta=0}$, i.e., significantly more than twice the particle density per nucleon. However, for the total charged multiplicity per incident nucleon one gains only a factor ~ 1.5 from $p + p$ to Au + Au. This shows that the particle population is especially enhanced in the central rapidity region, as one intuitively would expect. Figure 22(a) emphasizes this enhancement by displaying the ratio of charged particle pseudorapidity

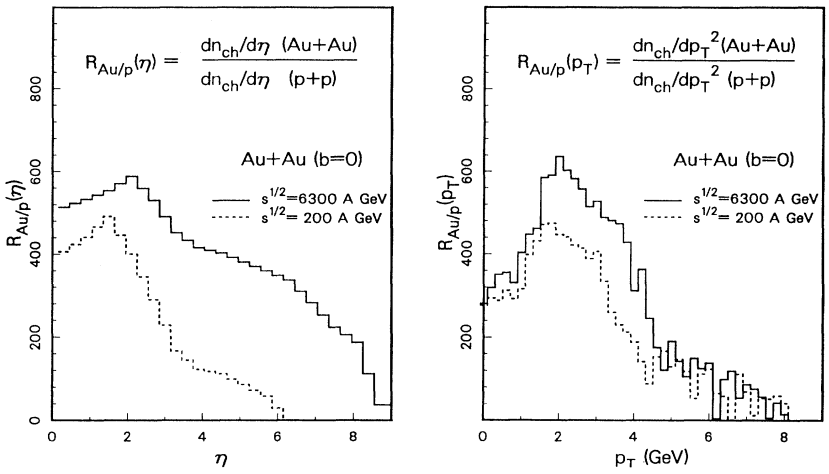

FIG. 22. The model results for the ratio of the inclusive charged hadron spectra of central Au + Au collisions to those of $p + p$ for $\sqrt{s} = 200A$ GeV (dashed histogram) and $\sqrt{s} = 6300A$ GeV (solid histogram). Both the ratio of pseudorapidity distributions (left) and the one of the transverse momentum distributions (right) were calculated with the space-time evolution scheme (e) defined in Sec. IV C and include the phenomena of nuclear shadowing, parton fusion and absorption, the Landau-Pomeranchuk effect, and soft gluon interference.

distributions

$$R_{Au/p}(\eta) = \frac{dn_{ch}/d\eta\,(Au + Au)}{dn_{ch}/d\eta\,(p + p)} \tag{42}$$

over the whole η range for the evolution scheme (e). The multiplicity increase in Au + Au collisions is particularly significant in the region $|\eta| \leq 2.5$ for $\sqrt{s} = 200A$ GeV and $|\eta| \leq 6$ for $\sqrt{s} = 6300A$ GeV.

Confronting the charged particle $p_\perp$ spectra of Au + Au collisions in Fig. 21 with the corresponding distributions in $p+\bar{p}$ collisions shown in Fig. 16(b), one observes a substantial suppression of high $p_\perp$ particle production in Au + Au relative to $p + \bar{p}$. For example, at $\sqrt{s} = 200A$ GeV, the $p_\perp$ distribution in Au + Au [(Fig. 21(a)] is of an exponential shape at least up to $p_\perp \simeq 5$ GeV, whereas the corresponding $p_\perp$ spectrum in $p+\bar{p}$ at $\sqrt{s} = 200$ GeV clearly exhibits a power law tail behavior already for $p_\perp \geq 3$ GeV. This feature is also reflected in Fig. 22(b) where the ratio

$$R_{Au/p}(p_\perp) = \frac{dn_{ch}/dp_\perp^2\,(Au + Au)}{dn_{ch}/dp_\perp^2\,(p + p)} \tag{43}$$

of the inclusive $p_\perp$ spectrum of charged particles in central Au + Au collisions to that of $p + p$ is plotted. One notices an enhancement in the hadron production of low and particularly of moderate $p_\perp$ particles which is peaked between $\sim$ 1.5 and 3 GeV. On the other hand, there is obviously a strong suppression of particles at large $p_\perp$ which is mainly due to the increased energy loss especially of high $p_\perp$ partons in the range $p_\perp$ =4–8 GeV. This phenomenon is due to multiple scatterings and gluon radiations and has been studied recently also by Wang and Gyulassy [2,3] who find qualitatively the same behavior. The observation of thermal shaped momentum distributions in Au + Au in contrast to clearly nonthermal spectra in $p+p$ at the same energy per nucleon is of particular relevance when asking to which degree the final hadron distributions can reflect a thermalization of the partons in heavy ion collisions. In fact, due to the extended time scale of a heavy ion reaction and the dense phase-space population of partons in the central region, the energy and momentum brought into the collision can quickly get distributed through frequent multiple interactions among the quanta [5,6]. As a consequence, the final charged particle spectra exhibit a resemblance with thermal distributions which is not noticeable in dilute and small sized systems as in hadron-hadron collisions.

V. SUMMARY

In this paper I intended to give a comprehensive presentation of a joint parton cascade–cluster hadronization approach to the space-time evolution and multiparticle production of ultrarelativistic nuclear collisions. The central objective was to introduce a phenomenological hadronization scheme that suits the specific concepts of the earlier developed parton cascade model and to link the perturbative QCD evolution of the parton distributions together with the nonperturbative description of hadron formation. The hadronization was modeled as a recombination of the final state partons at the end of the perturbative phase to form color singlet clusters, followed by the fragmentation "decay" of these clusters into observable hadronic states. It was demonstrated that the parton cascade model combined with this cluster hadronization scheme sets a consistent framework to simulate and study the time evolution of hadron-hadron and nucleus-nucleus collisions in complete phase space, from the first instant of collision to the final particle yield. The two fundamental parameters that define the boundary between the perturbative and nonperturbative descriptions in this model—the phenomenological invariant mass scale μ_0 and the fundamental QCD scale Λ—were fixed by comparison with experimental data from $e^+e^- \rightarrow$ hadrons. The model as a whole was then applied to $p\bar{p}$ collisions at $\sqrt{s}$ = 200–1800 GeV. It was shown that a satisfactory agreement with the data of the CERN and TEVATRON collider experiments can be achieved. The model results exhibited that perturbative QCD properties, leading to the production of multiple interacting parton cascades and minijets, play a dominant role for the particle production mechanisms at these ener-

gies. Finally, the model was used to investigate the reaction dynamics and hadron production in heavy ion collisions. Exemplarily the case of central Au + Au collisions at beam energies $\sqrt{s} = 200A$ GeV (RHIC) and $\sqrt{s} = 6300A$ GeV (LHC) was studied. Here the main interest was to illuminate the impact of a number of novel effects associated with the microscopic parton dynamics on the multiparticle production in these reactions. In particular, it was demonstrated by analyzing the model results for the momentum distributions of charged hadrons that nuclear shadowing, the Landau-Pomeranchuk effect, parton fusions and absorptions, and the destructive interference of soft gluons in the parton cascades lead to hadron spectra drastically different from the results of the naive calculation which neglects these effects. The most prominent feature is the strong reduction of the charged hadron yield by more than a factor of 3 in the central rapidity region. The predicted charged multiplicities in the central rapidity unit are $\simeq 1200$ for $\sqrt{s} = 200A$ GeV and $\simeq 2500$ for $\sqrt{s} = 6300A$ GeV. The ratio of charged to total multiplicity comes out to be $\simeq 0.6$. Furthermore it was concluded that in comparison with $p + p$ collisions at the same energies one gains a factor of about 2.5 per incident nucleon in the total multiplicities of particles produced in the central region. Also, the $p_\perp$ spectra of Au + Au relative to $p + p$ collisions show a considerable suppression of hadron production for $p_\perp \geq 4$ GeV, due to the aforementioned effects. In contrast to $p + p$, the hadronic momentum distributions in Au + Au exhibit a resemblance with thermal spectra which indicates the reflection of thermalization properties of the partons during the nuclear reactions. This may offer the possibility to learn about a quark gluon plasma phase transition from analyzing the hadronic spectra of ultrarelativistic heavy ion collisions.

ACKNOWLEDGMENTS

I would like to express very special thanks to J. Kapusta for his encouraging support in every respect and to B. Müller for his open ears. Furthermore I thank X. N. Wang for stimulating discussions and for providing a number of experimental data files from $p\bar{p}$ collisions. The numerical computations were performed on the two Cray computers of the Minnesota Supercomputer Institute and on a Silicon Graphics computer at Duke University. This work was supported by the U.S. Department of Energy under Contract No. DOE/DE-FG02-87ER-40328.

[1] See, e.g., B. Müller, *The Physics of the Quark Gluon Plasma*, Lecture Notes in Physics 225 (Springer, Heidelberg, 1985); L. McLerran, Rev. Mod. Phys. **58**, 1021 (1986); in *Quark Gluon Plasma*, edited by R. C. Hwa (World Scientific, Singapore, 1990); *Quark Matter '91*, Proceedings of the Ninth International Conference on Ultrarelativistic Nucleus-Nucleus Collisions, Gatlinburg, Tennessee, edited by T. C. Awes *et al.* [Nucl. Phys. **A544** (1992)].

[2] X. N. Wang and M. Gyulassy, Phys. Rev. D **44**, 3501 (1991).

[3] X. N. Wang and M. Gyulassy, Phys. Rev. Lett. **68**, 1480 (1992).

[4] K. Geiger and B. Müller, Nucl. Phys. **B369**, 600 (1992).

[5] K. Geiger, Phys. Rev. D **46**, 4965 (1992).

[6] K. Geiger, Phys. Rev. D **46**, 4986 (1992).

[7] R. D. Field and R. P. Feynman, Phys. Rev. D **15**, 2590 (1977); Nucl. Phys. **B138**, 1 (1978); R. P. Feynman, R. D. Field, and G. C. Fox, Phys. Rev. D **18**, 3320 (1978).

[8] B. Andersson, G. Gustafson, G. Ingelman, and T. Sjöstrand, Phys. Rep. **97**, 33 (1983); B. Andersson, G. Gustafson, and B. Söderberg, Nucl. Phys. **B264**, 29 (1986).

[9] D. Amati and G. Veneziano, Phys. Lett. **83B**, 87 (1979).

[10] A. Bassetto, M. Ciafaloni, and G. Marchesini, Phys. Rep. **100**, 203 (1983).

[11] D. Amati, A. Bassetto, M. Ciafaloni, G. Marchesini, and G. Veneziano, Nucl. Phys. **B173**, 429 (1980); G. Marchesini, L. Trentadue, and G. Veneziano, *ibid.* **B181**, 335 (1981).

[12] R. D. Field and S. Wolfram, Nucl. Phys. **B213**, 65 (1983).

[13] T. D. Gottschalk, Nucl. Phys. **B214**, 201 (1983); **B227**, 413 (1983).

[14] B. R. Webber, Nucl. Phys. **B238**, 492 (1984).

[15] G. Marchesini and B. R. Webber, Nucl. Phys. **B310**, 461 (1988).

[16] K. Geiger, "Nuclear and Medium Effects for Hadron Production in Ultra-relativistic Heavy Ion Collisions," University of Minnesota report, Minneapolis, 1992 (unpublished).

[17] B. Andersson, G. Gustafson, and B. Nilsson-Almquist, Nucl. Phys. **B281**, 289 (1987); B. Nilsson-Almquist and E. Stenlund, Comput. Phys. Commun. **43**, 387 (1987); B. Lörstad, Int. J. Mod. Phys. A **12**, 2861 (1989).

[18] M. Gyulassy, in *Proceedings of the Eighth Balaton Conference on Nuclear Physics*, edited by Z. Fodor (KFKI, Budapest, 1987); CERN Report No. CERN-TH-4794/87, 1987 (unpublished).

[19] K. Werner, Z. Phys. C **42**, 85 (1989).

[20] H. Sorge, H. Stöcker, and W. Greiner, in *Quark Matter '88*, Proceedings of the Seventh International Conference on Ultrarelativistic Nucleus-Nucleus Collisions, Lenox, Massachusetts, 1988, edited by G. Baym, P. Braun-Munzinger, and S. Nagamiya [Nucl. Phys. **A498**, 567c (1989)]; Ann. Phys. (N.Y.) **192**, 266 (1989).

[21] N.S. Amelin, E. F. Staubo, and L. P. Csernai, Nordita Report No. NORDITA-91-77, 1991 (unpublished); N. S. Amelin, E. F. Staubo, L. P. Csernai, V. D. Toneev, K. K. Gudima, and D. Strottman, Phys. Rev. Lett. **67**, 1523 (1991).

[22] T. W. Ludlam, BNL Report No. 51921, 1985 (unpublished); A. Shor and R. S. Longacre, Phys. Lett. B **218**, 100 (1989).

[23] T. Csörgö and J. Zimanyi, Hungarian Academy of Sciences (Budapest) Report No. KFKI-1990-37/A (unpublished).

[24] H. J. Mohring and J. Ranft, University of Leipzig Report No. UL-HEP-92-02 1992 (unpublished).

[25] See, e.g., R. P. Feynman, *Photon Hadron Interactions* (Addison-Wesley, Redwood City, CA, 1989).

[26] L. V. Gribov, E. M. Levin, and M. G. Ryskin, Phys. Rep. **100**, 1 (1983).
[27] European Muon Collaboration, J. Ashman *et al.*, Phys. Lett. B **202**, 603 (1988); European Muon Collaboration, M. Arneodo *et al.*, *ibid.* **211**, 493 (1988).
[28] S. J. Brodsky and H. J. Lu, Phys. Rev. Lett. **64**, 1364 (1990).
[29] A. H. Mueller and J. Qui, Nucl. Phys. **B268**, 427 (1986); J. Qui, *ibid.* **B291**, 746 (1987).
[30] F. E. Close, J. Qiu, and R. G. Roberts, Phys. Rev. D **40**, 2820 (1989); A. H. Mueller, Nucl. Phys. **B335**, 115 (1990).
[31] L. L. Frankfurt and M. I. Strikman, Phys. Rep. **160**, 235 (1988).
[32] M. Glück, E. Reya, and A. Vogt, Z. Phys. C **48**, 471 (1990).
[33] V. M. Belyaev and B. L. Ioffe, Nucl. Phys. **B313**, 647 (1989).
[34] D. Antreasyan *et al.*, Phys. Rev. Lett. **48**, 302 (1983).
[35] T. D. Gottschalk, CERN Report No. TH.3810-CERN, 1984 (unpublished).
[36] J. D. Bjorken, in *Current Induced Reactions*, Proceedings of the International Summer Institute on Theoretical Particle Physics, Hamburg, West Germany, 1975, edited by J. Körner *et al.*, Lecture Notes in Physics Vol. 56 (Springer, New York, 1976).
[37] A. H. Mueller, in *Quark Matter '88* [20], p. 41c.
[38] N. Abou-El-Naga, K. Geiger, and B. Müller, J. Phys. G **18**, 797 (1992).
[39] B. R. Webber, Annu. Rev. Nucl. Part. Sci. **36**, 253 (1986).
[40] G. Marchesini and B. R. Webber, Nucl. Phys. **B238**, 1 (1984).
[41] G. Altarelli, Phys. Rep. **81**, 1 (1982); G. Altarelli and G. Parisi, Nucl. Phys. **B126**, 298 (1977).
[42] L. D. Landau and I. Ya. Pomeranchuk, Dokl. Akad. Nauk SSSR **92**, 535 (1953); **92**, 735 (1953).
[43] M. Bengtsson and T. Sjöstrand, Nucl. Phys. **B289**, 810 (1987).
[44] M. Bengtsson, T. Sjöstrand, and M. van Zijl, Z. Phys. C **32**, 67 (1986).
[45] G. Marchesini and B. R. Webber, Nucl. Phys. **B349**, 617 (1991); S. Catani, F. Fiorani, and G. Marchesini, *ibid.* **B336**, 18 (1990).
[46] Note that color neutral systems need not be color singlets: for example, the color octet representation of $SU(3)_c$ contains two color neutral members, determined by the zero eigenvalues of the noncommuting generators τ_3 and τ_8. In the classical approximation, however, the final partons are statistically distributed among the possible $SU(3)_c$ representations. For example, a color neutral $q\bar{q}$ pair has a probability $\frac{1}{2}$ to be a color singlet and a probability $\frac{1}{2}$ to be a color octet.
[47] T. Sjöstrand, Comput. Phys. Commun. **28**, 227 (1983).
[48] JADE Collaboration, W. Bartel *et al.*, Z. Phys. C **33**, 23 (1986); S. Bethke, Habilitation thesis, LBL Report No. 50-208, 1987 (unpublished).
[49] Another candidate for the measure of the two-particle phase-space separation is $\Delta'_{ij} = r^{\mu}_{ij} p_{ij,\mu}$. This form seems at first sight to be the most natural choice. However, it is absolutely inappropriate, because it correlates the particles' positions and momenta. For any two particles 1 and 2 with their relative distance vector $\mathbf{r}_{12}$ perpendicular to their relative momentum $\mathbf{p}_{12}$ one has $\Delta'_{12} = 0$, independent of their distance of separation or their relative motion. Consider the extreme example of two particles with equal energy but moving ten miles apart from each other with opposite momenta. Such a configuration certainly does not meet the criteria for a minimal phase-space separation.
[50] H. U. Bengtsson and T. Sjöstrand, Comput. Phys. Commun. **46**, 43 (1987).
[51] M. M. Block and R. N. Cahn, Rev. Mod. Phys. **57**, 563 (1985); and in *Physics Simulations at High Energy*, edited by V. Barger, T. Gottschalk, and F. Halzen (World Scientific, Singapore, 1987).
[52] S. L. Wu, Phys. Rep. **107**, 59 (1984); Mark J Collaboration, B. Adeva *et al.*, *ibid.* **109**, 131 (1984); B. Naroska, *ibid.* **148**, 67 (1987).
[53] In the γ rest frame, the q and $\bar{q}$ move apart in opposite directions, both initiating timelike cascades which evolve independently in free space until they hadronize after a time $t_h \sim 1/\mu_0$. Since there are no surrounding partons present in this case, parton-parton collisions and absorption processes are absent, and accordingly there is no suppression of radiative gluon emissions associated with the Landau-Pomeranchuk effect. Hence, for e^+e^- annihilation, the space-time evolution of parton cascades in this model reduces to the standard description of coherent QCD jet evolution (see, e.g., Refs. [39]).
[54] J. D. Bjorken and S. J. Brodsky, Phys. Rev. D **1**, 1416 (1970).
[55] S. Brandt, C. Peyrou, R. Sosnowski, and A. Wroblewski, Phys. Lett. **12**, 57 (1964); E. Farhi, Phys. Rev. Lett. **39**, 1587 (1977).
[56] R. Brandelik *et al.*, Phys. Lett. **86B**, 243 (1979).
[57] C. Berger *et al.*, Phys. Lett. **86B**, 413 (1979); **86B**, 418 (1979); **81B**, 410 (1979).
[58] R. Brandelik *et al.*, Phys. Lett. **89B**, 418 (1980).
[59] R. Brandelik *et al.*, Z. Phys. C **4**, 87 (1980).
[60] R. Brandelik *et al.*, Nucl. Phys. **B148**, 189 (1979).
[61] G. G. Hanson, in *Gauge Theories and Leptons*, Proceedings of 13th Rencontre de Moriond, 1978, edited by J. Tran Thanh Van (Editions Frontières, Gif-sur-Yuette, France, 1978).
[62] C. Berger *et al.*, Phys. Lett. **78B**, 176 (1978); **81B**, 410 (1979).
[63] W. Bartel *et al.*, Phys. Lett. **88B**, 171 (1979).
[64] R. Brandelik *et al.*, Phys. Lett. **89B**, 418 (1980).
[65] M. Althoff *et al.*, Z. Phys. C **14**, 5 (1983), and references therein.
[66] A. Capella, U. Sukhatme, and J. Tran Thanh Van, Z. Phys. C **3**, 329 (1980); J. Ranft, Phys. Lett. B **188**, 379 (1987); Phys. Rev. D **37**, 1842 (1988); F. E. Paige and S. D. Protopopescu, in *Physics of the Superconducting Super Collider*, Proceedings of the Summer Study, Snowmass, Colorado, 1986, edited by R. Donaldson and J. Marx (Division of Particles and Fields of the APS, New York, 1987); T. Gaisser and T. Stanev, Phys. Lett. B **219**, 375 (1989).
[67] T. Sjöstrand and M. van Zijl, Phys. Rev. D **36**, 2019 (1987).
[68] X. N. Wang and M. Gyulassy, Phys. Rev. D **45**, 844 (1992).
[69] UA5 Collaboration, G. J. Alner *et al.*, Phys. Rep. **154**, 247 (1987).
[70] UA2 Collaboration, M. Banner *et al.*, Phys. Lett. **122B**, 322 (1983).

[71] UA1 Collaboration, C. Albajar *et al.*, Nucl. Phys. **B309**, 405 (1990).
[72] F. Abe *et al.*, Phys. Rev. Lett. **61**, 1819 (1988).
[73] UA5 Collaboration, G. J. Alner *et al.*, Z. Phys. C **33**, 1 (1986).
[74] F. Abe *et al.*, Phys. Rev. D **41**, 2330 (1990).
[75] UA5 Collaboration, G. J. Alner *et al.*, Nucl. Phys. **B291**, 445 (1987).
[76] UA5 Collaboration, R. E. Ansorge *et al.*, Z. Phys. C **43**, 357 (1989).
[77] See, e.g., U. Heinz, K. S. Lee, and E. Schedermann, in *Quark Gluon Plasma* [1], p. 471, and references therein.